Quantitative Non-Destructive Testing

Annual Report
May 1, 1984 - April 30, 1985
for
Cooperative Agreement NCCI-50

C. S. Welch, Principal Investigator
Department of Physics,
College of William and Mary
Williamsburg, Virginia 23185

to

NASA Langley Research Center
Hampton, Virginia 23665

(NASA-CR-176761) QUANTITATIVE NON-DESTRUCTIVE TESTING Annual Report, 1 May 1984 - 30 Apr. 1985 (College of William and Mary) 43 p HC A03/MF A01 CSCL 14D

N86-25001

Unclas
G3/38 42907

Quantitative Non-Destructive Testing May 1, 1984 - April 30, 1985

Executive Summary

The work undertaken during this period included two primary efforts. The first is a continuation of theoretical development from the previous year of models and data analyses for NDE using the OPTITHIRMS system, which involves heat injection with a laser and observation of the resulting thermal pattern with an infrared imaging system. The second is an investigation into the use of the thermoelastic effect as an effectove tool for NDE. As in the past, the effort is aimed towards NDE techniques applicable to composite materials in structural applications.

The theoretical development started from the ideal cases described earlier and produced several models of temperature patterns over several geometries and material types. Agreement between model data and temperature observations was obtained. A model study with one of these models investigated some fundamental difficulties with the proposed method (the primitive equation method) for obtaining diffusivity values in plates of finite thickness and supplied guidelines for avoiding these difficulties. A wide range of computing speeds was found among the various models, with a one-dimensional model based on Laplace's integral solution being both very fast and very accurate.

Thermoelastic experiments were successfully performed on a stainless steel plate with a hole in the center, and some relevant system characteristics were obtained. A literature review found related activity in several other places including foreign countries. One of these activities has led to a commercially available device for making thermoelastic stress measurements, and a demonstration was held. A possible application to NDE in previously strained materials was suggested by the data. The situation for graphite-epoxy composites was found to be complex both experimentally and theoretically compared to that for metals, and directions for further study are suggested.

Annual Report - May 1, 1984 - April 30, 1985
for
Quantitative Nondestructive Testing
by
C. S. Welch

1.0 Introduction

This report discusses the work done under NASA Cooperative Agreement NCCI-50 with the Physics Department of the College of William and Mary for the contract year from May 1984 through April 1985. As none of the work has been contained in progress reports for portions of this period, this report will cover the topics included in a complete manner.

The scope of the reported work includes two primary efforts. The first is theoretical support of the OPTIcal THermal Infra-Red Measurement System (OPTITHIRMS), which is being developed at NASA Langley for non-destructive examination of structural materials using infra-red radiative techniques and extensive computer-based data analysis of the resulting measurements. The emphasis of this work is on graphite-epoxy composite materials. The second effort involves the use of the thermoelastic effect to examine stresses in materials undergoing cyclic, controlled loading, with the goal of identifying flawed and weakened portions of structures prior to failure. This effort is also focused on applicability to graphite-epoxy structures. It has both theoretical and experimental elements.

2.0 Thermal Models and Diffusivity Estimates

The present configuration of the OPTITHIRMS produces a heated area on the surface of a sample by irradiating it with a carefully scanned beam from an infrared laser, The heat pattern thus produced is radiatively detected with a scanning infrared imager, and the image data is digitized and stored for later analysis. To date, this system has been applied to estimates of the diffusivity of a material from the time evolution of the resulting temperature pattern.

The models developed to date have been in support of this effort. In the previous year, the models consisted of analytical models for simple geometries, and the emphasis was on qualitative issues, such as sensitivity as a function of dimensionality and appropriate non-dimensionalizations of the conduction equation. It was found that if time is scaled to the pulse time of heat input, a natural spatial scale is generated by combining the time scale with the material diffusivity. In infinite or semi-infinite media, the heating curves for point sources then reduce to products of physical constants, such as emissivity, heat capacity and pulse power, and universal functions of scaled time and space. These functions were derived and illustrated for configurations with dimensionalities of 1,2 and 3. The effort during the current year was to apply these idealized heating curves to experimentally observed data.

The computer techniques used to formulate these models were more sophisticated than those for the previous year. In the previous year, the formulas were obtained in closed form in terms of standard transcendental mathematical functions. Numerical computations were used to evaluate polynomial approximations to these functions at desired points in time and space. In the present year, the source functions became distributed, and additional numerical techniques were used to sum partial temperatures over the source at each desired response point for a given value of time. The models

thus constructed are termed numerical integration models.

In the area of data analysis, the first estimate of diffusivity of a material was obtained by image analysis based of evaluation of terms directly from the differential equation for heat conduction. The method of calculating diffusivity directly from estimates of terms in the governing equation is called the primitive equation method. As experimental use of this method was found to be difficult, a model study was undertaken to examine the application of the primitive equation method to plates of finite thickness, and guidelines for controllable experimental parameters required to obtain accurate diffusivity values were obtained.

2.1 Line scan models

The motivation for the line scan model was to synthesize a temperature field from theoretical considerations which would be directly comparable to radiometric data obtained from the OPTITHIRMS system. For this purpose, motivated by considerations of theoretical simplicity, experimental simplicity, and closeness of correspondence, the situation chosen was the surface temperature distribution on the face of a thick sample of stainless steel on which a short, straight line of heat was injected with the laser. The surface of the stainless steel was coated with a high-emissivity coating (emissivity > .99) to boost signals, but the coating was thin enough that viewed temperature corresponded closely with surface temperature of the sample. Experimental durations were chosen to be short enough that the sample appeared semi-infinite, with reflections from the sides and back being well below the limits of detection. The short line was chosen to boost the maximum temperature attained in the heated area, again to boost the signal level. The model assumed a Gaussian distribution for the beam profile. Parameters for the model included beamwidth, line length, line position and orientation, pulse duration, input power, sample emissivity, image scale, and image time. Material properties required were thermal diffusivity, conductivity, and volumetric heat capacity. Calculations were obtainable over both the heating and cooling phases of the experiment.

The model, based on the three-dimensional point source equation, divided the image surface into its individual pixels (squares of size Δ) and treated each of these as a point source located at the pixel center. The continuous local variables, x and y, thus became referenced in integral blocks of size Δ with integer variables I and J respectively. The temperature at the (I,J)'th block thus was represented by the sum of partial temperatures from each (K,L) block with non-negligible heating intensity, represented by the intensity at the center of the block $\mathbb{I}(x_K, y_L)$, with $x_K = \Delta(K - 1/2)$ and $y_L = \Delta(L - 1/2)$. With these definitions, the distance between a source point and an observation point is given as $r_{IJ,KL} = \Delta[(I-K)^2 - (J-L)^2]^{1/2}$. The temperature is thus formally represented as:

$$T_{IJ} = \sum_{KL} \frac{\Delta^2 \mathbb{I}(X_K, Y_L)}{2\pi K r_{IJ,KL}} \left\{ \operatorname{erfc}\left(\frac{r_{IJ,KL}}{\sqrt{4kt}}\right) - U(t-t_{off}) \operatorname{erfc}\left(\frac{r_{IJ,KL}}{\sqrt{4k(t-t_{off})}}\right) \right\}$$

in which the source is pulsed between times (t) zero and t_{off} and U is the Heaviside step function. In local coordinates, with the zero in the center of the source line, which extends in the y direction for a total distance of L, and has a scale width of w. the source intensity function is

$$\mathbb{I}(x,y) = \frac{P}{2\sqrt{\pi}wL}\exp(-(x/w)^2)\left[\operatorname{erfc}\left(\frac{y-L/2}{w}\right)-\operatorname{erfc}\left(\frac{y-L/2}{w}\right)\right]$$

This formulation is appropriate except when I=K and J=L, the response pixel and the source pixel being the same. In this case, the value of $r_{IJ,KL}$ becomes zero, and the corresponding term becomes infinite. The artifice of assigning some nominal value to this case and letting the pixel size become very small is not satisfactory because convergence is very slow and, particularly for short times, local temperature is primarily due to local heating. Thus, the model must be altered in this case, and the most reasonable alteration is to abandon the notion of a point source and spread the integration somehow over the local pixel. In doing this, because only the local pixel is considered and because the pixel size is generally much smaller than the scale length for the Gaussian source ($\Delta/w \ll 1$), it is also appropriate to use the asymptotic time-independent formula for temperature distribution within the pixel and to consider the intensity within the pixel to have a constant value equal to the value at the pixel center, **I**. Here, use is made of the concept, valid only in three-dimensional geometries, that the temperature pattern asymptotically approaches a time-independent shape rather than increasing without limit under constant heat input. With a constant source intensity limited to a finite region, the formulation of Lax [1977] shows the temperature at an observation point to be proportional to the average of the reciprocal distance between observation and source averaged over the source region. This average may be denoted <1/r>. The temperature contribution calculated in this manner is not suitable as a representative contribution to the total heating pattern from the local pixel because it depends on the particular position of the observation point within the pixel. To obtain a representative contribution, it is necesary to average this temperature over all of the observation points within the pixel, an operation denoted by <<1/r>>. For a square pixel with sides of length Δ, the formula for <<1/r>> is

$$\langle\langle 1/r \rangle\rangle = \frac{1}{\Delta^4}\int_0^\Delta\int_0^\Delta\int_0^\Delta\int_0^\Delta \frac{d\xi\, d\eta\, dx\, dy}{[(\xi-x)^2+(\eta-y)^2]^{1/2}}$$

The family of integrals in this expression, which can be called I^Δ, can be expressed in terms of a single member I^1 with the scaling expression $I^\Delta = \Delta^3 I^1$. This integral was evaluated in an approximate manner by reducing it to a sum of integrals over subvolumes of side 1/N. Only a small number of these integrals contain the singularity, and these can be expressed in terms of I^1. If this is done and the remainder of the integrals are approximately evaluated as the product of their 4-dimensional volume and the central value of the integrand, the formula

$$I^1(1-1/N) = \lim(N \to \infty) S_N/N^3, \text{ with } S_N = \sum_i{}' \sum_j{}' \sum_k \sum_l [(i-k)^2-(j-l)^2]^{-1/2}$$

results, the primes on the sums denoting that the singular terms (those with i=k and j=l) have been removed. After further manipulation to consolidate the number of summations from 4 to 2, the expression was evaluated for an increasing series of values for N up to N=500, and an approximate value of $I^1 = 2.971$ was obtained as the asymptotic value approached for large N. This value was then used to provide the representative value for the singular pixel during the period of heating. A different approximation was necessary within this pixel to account for partial temperature contributions during cooling ($t > t_{off}$), for the use of the asymptotic value in the difference formula which

applies following the pulse results in zero contribution to the local pixel from heat applied at the same pixel. To make this approximation, the error function terms in the point source expression were expanded in Taylor Series to second order in their local times. As expected, the first order terms summed to zero, leaving a contribution at second order.
This resulted in the formula:

$$T_{p,ij,ij} = \frac{I\Delta^2}{4\pi^{3/2}Kk^{1/2}}\left[\frac{1}{\sqrt{t-t_{off}}} - \frac{1}{\sqrt{t}}\right]$$

for the partial temperature at a pixel identical with the source pixel at a time subsequent to the end of the laser pulse. Inspection of this formula reveals that at the moment following the end of the pulse, the partial temperature from this formulation again becomes infinite. Thus, there is a "blind time" in the model for a short period following the pulse. This blind time corresponds to the time prior to the establishment of the asymptotic time-independent temperature within the pixel. The blind time was estimated as the time for the contribution at the source pixel following the pulse to equal the contribution immediately before the end of the pulse. This equality leads to an estimate of the blind time of the same order as $\Delta^2/100k$. For stainless steel and the .0115 cm pixel size considered in the verification effort, the blind time was on the order of .0001 s. With a frame time of .03 s, the blind time for the verification was considered unimportant for all frames following the first after the visible laser pulse.

Model formula development thus resulted in three separated cases, which provided a complete description of the temperature evolution in a descrete grid, with the exception of a short time, the "blind time", following the end of the pulse of heat input. The formulas describe, respectively, the contribution for all pixels for which source and response locations are not identical, the case of identical source and response pixels during the time of the pulse, and the case of identical source and response pixels during the time following the pulse. An additional formula describes the duration of the blind time following the pulse.

Model construction, using these formulas, was first done on a grid of 480 pixels vertically and 512 pixels horizontally, to correspond to the digitized image data. In order to construct an evaluation algorithm, one further issue needed resolution. The integrals in the Green's function evaluation have infinite limits, a clearly impossible situation for numerical evaluation of sums. It becomes necessary, then, to describe a finite set of pixels for summation by identifying a locale within which all of the source pixels which have a significant effect on a given response pixel are located. At the same time, a criterion for "having a significant effect" needs to be defined, for if the effect is too small, the underflow errors will occur during the calculation, and computer time will be devoted to calculating insignificant contributions. For the heat equation, this task is simplified somewhat, as the temperature resulting from a given localized heat input decreases monotonically with distance in all directions from the source. In the homogeneous material covered by this model, the requirement may be met by defining a "radius of significance" around each source point beyond which the heat from the source has no significant effect. Sources are only considered if they are closer to the response point under consideration than the radius of significance. This criterion would be sufficient if all source points had equal intensity, but this is clearly not the case for the laser line scan considered by the model. There is, in addition, a region around the source outside of which no significant heat is added to the sample. From the iso-intensity curves surrounding the source function, this region is seen to have the shape of a capsule with sides parallel to the laser scan and semi-circular "end caps". For a given response pixel, contributions to the

temperature rise are computed only for source pixels located within both the capsule around the laser line and circle with the radius of significance around the response point. When the two regions have no intersection, the calculation is terminated. In addition, the calculation is limited to those response pixels lying within a "window of interest", chosen as the area within the digitized image. For the model, the radius of significance was defined in terms of a user-chosen permitted fractional error. The region chosen was the smallest set of pixels which completely covered the circle outside of which the total fractional response was equal to the permitted error fraction. The source capsule was chosen to be the smallest set of pixels covering the iso-intensity contour outside of which the total fractional incident power is equal to the permitted fractional error.

The model which evaluated these equations subject to these constraints for a given user-chosen laser line and material was written in FORTRAN 77 as a program called LINETEMP with its associated subroutines. The program is resident on the MCIS VAX and on backup tapes. A further discription is given in Appendix 1. The output of the model is a single file containing the calculated temperature field as an array of real numbers, with associated date, time and array size values. This file was written to be commpatible with a conversion program to put it into SADIE (The image analysis and display package resident of the MCIS VAX) format for display and further analysis.

A significant property of the program was its running time on the MCIS VAX 750 in timesharing mode. The verification run involved a line pattern with a length of about 240 pixels, half the height of the image window, and a width of about 100 pixels, about 20% of the image window width. The evaluation of this image required about 50 hours of computer time, clearly too much for practical application. On analysis of the operation time, over 95% was associated with forming the sums, with the other 5% or so used in evaluating the expressions in the formulas. The time-consuming element in summation was "page faults", the disk accesses required in a "virtual memory" computer for obtaining values separated too far in address space. This separation distance is directly a function of the size of the arrays used in the model. To ameliorate this situation, the model was reduced in resolution by a factor of 4, to produce a region of interest 128 pixels by 120 pixels. This reduction, besides providing substantial increases in speed, is compatible with the manufacturer's specifications for the number of independent data points sampled over an image by the infrared imager. The expected running time was estimated to be proportional to the number of term in the sums. For a given image, the number of terms is proportional to the fourth power of the resolution. Reducing the resolution by a factor of 4 was thus expected to reduce the run time by a factor of 256 to about 12 minutes. The actual runtime attained was about 6 minutes, the further reduction being attributed to a smaller number of disk accesses required with the smaller (1/16th the original size) arrays. Further reduction could reasonably be expected by reconfiguring the runtime environment of the model to provide more main memory during operation.

For model verification, data were taken from a short line scan of a block of stainless steel, and the model was run for nominal laser and stainless steel parameters corresponding to the experimental conditionss. The data were limited in value by the absorbtion of heat in the stainless steel sample, resulting in a relatively low signal to noise ratio. In order to obtain a reduction in noise, a band was averaged across the transverse part of the image to include 60 original points in each of the averages. The temperature scale was not available in the data, so the range of averaged temperatures was set equal to the temperature range in the model. The central positions were likewise estimated from the image data. The resulting model verification data are shown in Figure 2.1. In this figure, the temperature profile of the data is seen to compare closely with that of the model.

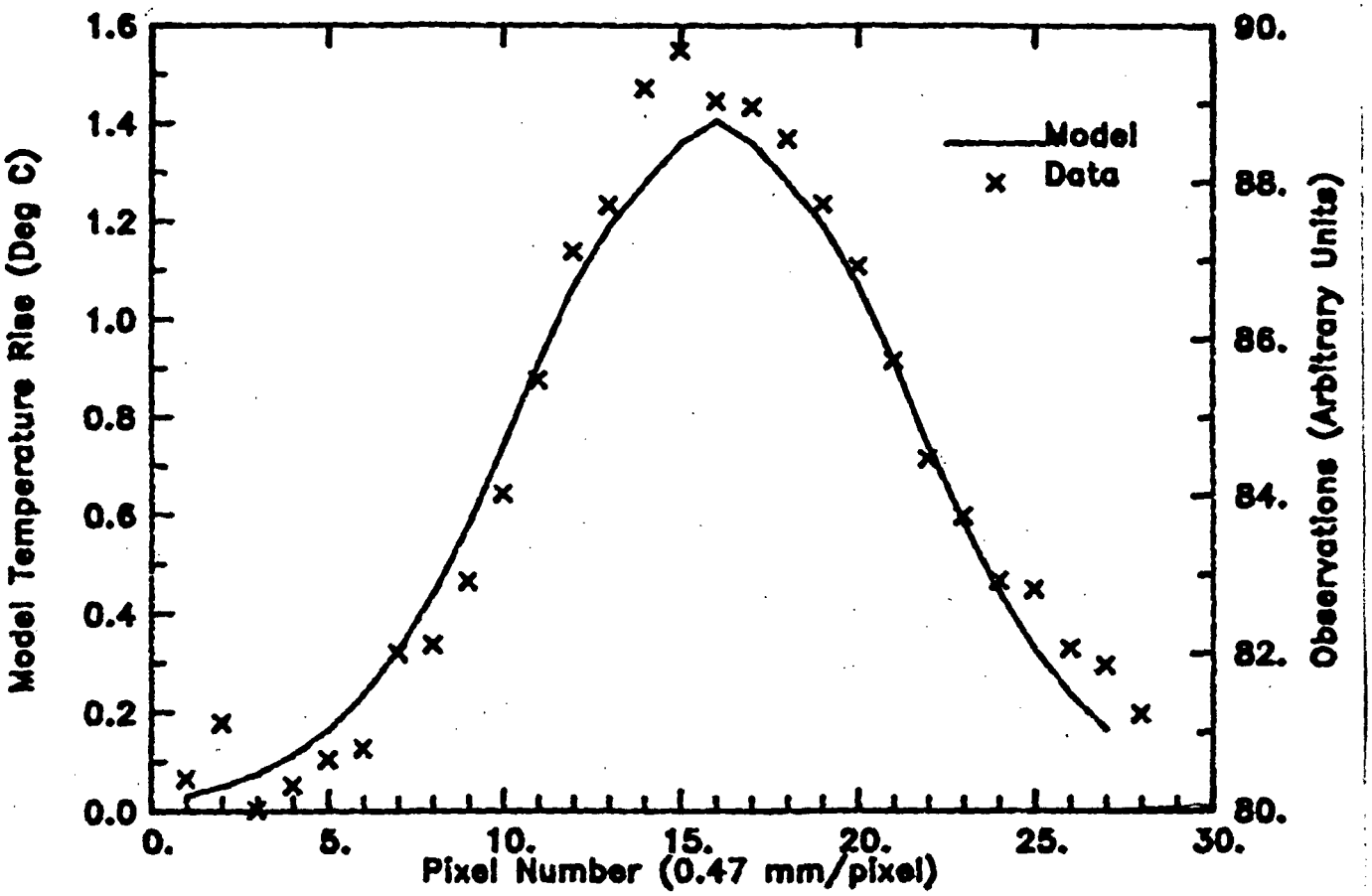

Figure 2.1. Comparison of data and line scan model for stainless steel thick sample. Comparison is between a transverse profile of the image data comparably extracted from both model and data images. Variations between the model and the data are within the limits expected from noise in the observations.

The thin plate situation has several advantages over the thick sample case. The temperature distribution from a given source continues to increase with irradiation time, rather than reaching an asymptotic limit, so the temperature contrast in an image can be increased simply by increasing pulse length. Also, the distribution of heat within the sample equilibrates throughout the thickness of the sample in a time of order L^2/k following the cessation of thermal input, where L is the sample thickness and k is its diffusivity. Thus, the temperature distribution throughout the sample subsequent to this time is completely determined by the surface temperature distribution. This permits specification of the thermal state of an object from sets of measurements by the same thermal imager over time, eliminating the requirement for consistent measurements of laser pulse characteristics and material emissivity and the implied associated requirement for intercalibration of diverse sensors. Further simplification is attained by placing a laser stripe on the thin plate, for then the situation is reduced to one spatial dimension if the sample is homogeneous. Finally, the reduction in dimensionality permits models to describe the thermal field to within a given resolution and acccuracy with greatly decreased runtimes. As will be shown is subsequent reports, these advantages have permitted considerable progress using linear heat patterns on thin plates.

During the period covered by this report, a model called TLINE was written to use an initial one-dimensional set of temperature data as its input and produce sets of temperature predictions at times subsequent to the initial

data time as its output in the case of a cooling thin plate following a line-scanned input. The basis for the model is Laplace's solution of the one-dimensional heat equation for an infinite solid, adapted from Carslaw and Jaeger [1959, eq 2.2(1)] as:

$$T(x,t) = \frac{1}{2\sqrt{(\pi kt)}} \int_{-\infty}^{\infty} T(x',0) \exp(-(x-x')^2/4kt)\, dx'$$

where x is position in the one-dimensional space, k is diffusivity of the material, and t is the time since the initial conditions were observed. In evaluating this integral, the spatial coordinate is divided into intervals of common length Δ, so that the distances (x-x') all become integral multiples of Δ, $j\Delta$. Then all of the arguments of the exponentials become j^2 powers of a common factor, $F_1 = \exp(-\Delta^2/(4kt))$ and the sum strongly resembles a convolution sum. Finally, an iteration scheme was used by which all of the factors can be constructed from products of previous factors, the result being that the exponential function need only be called once for each calculation time. The single set of exponential factors and the iterative calculation of these factors with only a single evaluation of the exponential function both save considerable computer time. Further time could be saved if the sums were cut off after the terms become smaller than some cut-off value, but this strategem has not yet been implemented in this model. With real data, values of the initial conditions do not extend to infinity, of course. Still, some value needs to be supplied to the formula beyond the ends of the line at long times to approximate these unknown values, or else the ends of the line will start to exhibit artifacts. In TLINE, the option exists for specifying a constant value to be assumed for the initial temperature beyond the ends of the data. If a value of zero is supplied, the program uses the end data points for the constant value.

In tests against a Gaussian curve, TLINE reproduced the analytic values to better than 1 part in 10^6 under the main peak. In the edges, artifacts of up to .005 degrees have been found out of values on the order of 10 degrees. This numerical accuracy is presently greater than the experimental data by several orders of magnitude, so further refinement seems inappropriate at this time. Running time for a single time prediction of 256 points on the VAX 750 in MCIS is 1.7 seconds. Because it requires only one parameter, diffusivity, and makes few assumptions about the input data, program TLINE should prove useful whenever temperature data are to be predicted in one-dimensional situations from previously existing temperature data. Tests have shown that the algorithm is not suited for back-prediction, as small perturbations grow very quickly to dominate the solution.

2.2 Point source temperature distribution

Work from the previous year showed that the time evolution of a point source in a three-dimensional, semi-infinite medium approaches an asymptotic spatial distribution varying as the inverse of the distance from the source. With a real beam, having its intensity distributed over some finite area, this implies that the central temperature in the heated zone will approach some finite value, as shown by Lax [1977]. For a given beam shape, the attained temperature is thus dependent only on the total intensity, which can be controlled very precisely with laser sources and presicion attenuators. This precise control of the maximum attainable temperature has important implications in the materials processing industry. It can also be used in the context of NDE for purposes of calibration as well as for thick sample

scanning. To exploit this feature fully, it is desired to obtain an expression for the radial dependence of the asymptotic temperature profile rather than simply its peak value. To this end, the starting point is the point source temperature distribution in a semi-infinite three-dimensional medium, given by Carslaw and Jaeger [1959, eq 10.4(2)]:

$$T = \frac{P}{2\pi Kr}\ \mathrm{erfc}\left(\frac{r}{\sqrt{4kt}}\right)$$

As time approaches infinity, the complementary error function approaches unity, reducing the functional dependence of the temperature from a point source to only the input power and the distance from source to observation point. The calculation of the asymptotic temperature distribution from a distributed source is accomplished by weighting the inverse distance from each source point to a given response point by the power density at the source point and integrating over the entire source pattern. For a circular Gaussian source pattern with a halfwidth of w, Lax [1977] expresses the result as

$$T = T_{max} N(R, Z, \infty)$$

where R and Z are the radial distance and depth normalized by the source halfwidth: R = r/w, Z = z/w. The third parameter in the N function is related to the absorbtion depth of the incoming radiation. Its infinite value corresponds to surface absorbtion, the usual assumption in NDE of structural materials. With this notation, $T_{max} = P/(2\sqrt{\pi}Kw)$ incorporates the direct effects of the power and the beam width, K being thermal conductivity of the material, while N is a function of the non-dimensional position. The image of the heated spot is due only to surface temperature, so our interest is in $N(R,0,\infty)$. From Lax [1977], this function is the ratio of two integrals,

$$N(R,0,\infty) = \frac{\int_0^\infty J_0(\lambda R)\exp(-\lambda^2/4)\,d\lambda}{\int_0^\infty \exp(-\lambda^2/4)\,d\lambda}$$

The numerator is evaluated using the tables of Gradshteyn and Rhzhik [1980, eq 6.618], while the denominator is a common form. On evaluation of N and substitution of the expression for T_{max} the asymptotic variation of the temperature from a Gaussian spot is given as

$$T = \frac{P}{2\sqrt{\pi}Kw}\exp\left(-\frac{r^2}{2w^2}\right) I_0\left(\frac{r^2}{2w^2}\right)$$

where I_0 is the zero order modified Bessel function of the first kind. This particularly simple form for the limiting temperature distribution from a Gaussian heat source in a thick material has not previously been reported. Its numerical evaluation is relatively fast, for the modified Bessel function is well described by a 6 term polynomial in the square of the argument for small arguments, while for large arguments, the product of the modified Bessel Function and the exponential function are well described by a 9 term polynomial [Abramowitz and Stegun, 1965, eq 9.8.1, 9.8.2].0

2.3 Point source model and Diffusivity Estimates

The development of a "point source model" was undertaken in order to examine the application of the primitive equation technique with the thin plate assumption for estimating diffusivity in plates of finite thickness. The approach taken was a Green's Function approach similar to that for the line scan. Considerable computation was saved, however, by calculating the resulting temperature only along a single radius, the material under consideration being homogeneous and the source radially symmetrical. The sample thickness is taken into consideration by constructing a series of image sources, each of which adds to the temperature at a point within its region of influence. Because of this method of construction, the point source model is applicable both to plates of finite thickness and to very thick plates. It is coded as program POINTEMP, and has as output a time series of temperatures between two chosen times and at a chosen time interval between two chosen radial distances at a chosen radial interval.

The method of diffusivity estimation used during the first part of the contract year was direct evaluation of ratios of temperature derivatives in the heat equation itself. This method is known as the primitive equation method, to identify it among several methods which have since been introduced. From the experimental side of the effort, the question of how long the source should be left on to obtain good diffusivity estimates was posed. The answer to this question divides into two parts. The first part concerns the temperature field itself and addresses estimation issues associasted with uncertainty in signal levels and souces of noise. The second part of the answer concerns applicability of the formulation itself: In a plate of finite thickness, under what conditions does the ratio of observed temperature derivatives approximate the material diffusivity? It is the second part of the answer which motivated the model development.

The first approach to this answer was to construct an analytical expression for the temperature on a finite-thickness plate from a series of point sources, the real source and the set of image sources associated with the three-dimensional distribution of temperature in an infinite medium which, taken as a sum, satisfy the adiabatic boundary conditions used for the flat plate. The only difference between the total solution to the heat equation and that obtained by evaluating terms visible on the surface only is that the depth dependence of the temperature is neglected in the evaluation of the surface evaluation. The ratio of surface-evaluated to true diffusivity is the ratio of the entire Laplacian to the 2-dimensional (surface) Laplacian. The actual calculation for the error was that of the ratio of the difference of these two to the entire Laplacian. The expectation with this approach was that a set of lines could be constructed in the position-time domain each of which corresponded to a given error, say 5%,1%,.1% ..., and that at long times following the laser pulse, as the temperature field equilibrated through the plate thickness, the error would asymptotically approach zero. The result was different from this expectation. It showed that for any chosen distance from the source, the error never fell below some finite value, and that this value increased monotonically on approaching the source point. Stated differently, it showed that there was no finite region where diffusivity could be determined with any desired accuracy simply by waiting longer for the temperature to equilibrate through the plate thickness.

The way to reconcile the non-convergence of the point source analysis with the seemingly trivial identity in the two-dimensional case seemed to be to distribute the energy in the point source over some finite area on the plate and rerun the image solution with sources distributed over the image planes rather than point sources. Because the difficulty was considered to be associated with the singular nature of the point source, distributed sources with continuous derivatives were expected to cure the problem. A source distribution with Gaussian form would not only satisfy this criterion, but would also correspond to the best available estimate of the distribution in the actual laser beam used in the experiments. Thus the error estimates

obtained from the numerical results would be directly applicable to the experimental situation. A search of the literature revealed no analytic way of adding solutions to the heat equation at layers of images with Gaussian distribution, so a numerical model was called for. The resulting model was developed in a program named POINTEMP.

During the time that the theoretical work had been going through these phases without producing a satisfactory answer to the question of how long to make the laser pulse, the experimental part of the work moved to the use of line scans rather than point scans. An exhaustive survey of parameter space with POINTEMP was considered relatively unimportant compared with work on models with line sources, so only a qualitative survey was done with POINTEMP and its diffusivity estimator, CALCK. The diffusivity estimator uses a numerical approximation to the time derivative and the Laplacian from the radial data produced by POINTEMP. The only notable feature of CALCK is that the time derivative estimator is fashioned to use the same data values with the same weights as the Laplacian estimator. Thus no errors in calculated diffusivities are attributable to an offset in the locus of the two estimates. The estimates employ six points in radius-time space and may be considered as centered at the central of three spatial points and halfway between the two time points. Figure 2.2 shows the results of a single run of POINTEMP and CALCK for stainless steel.

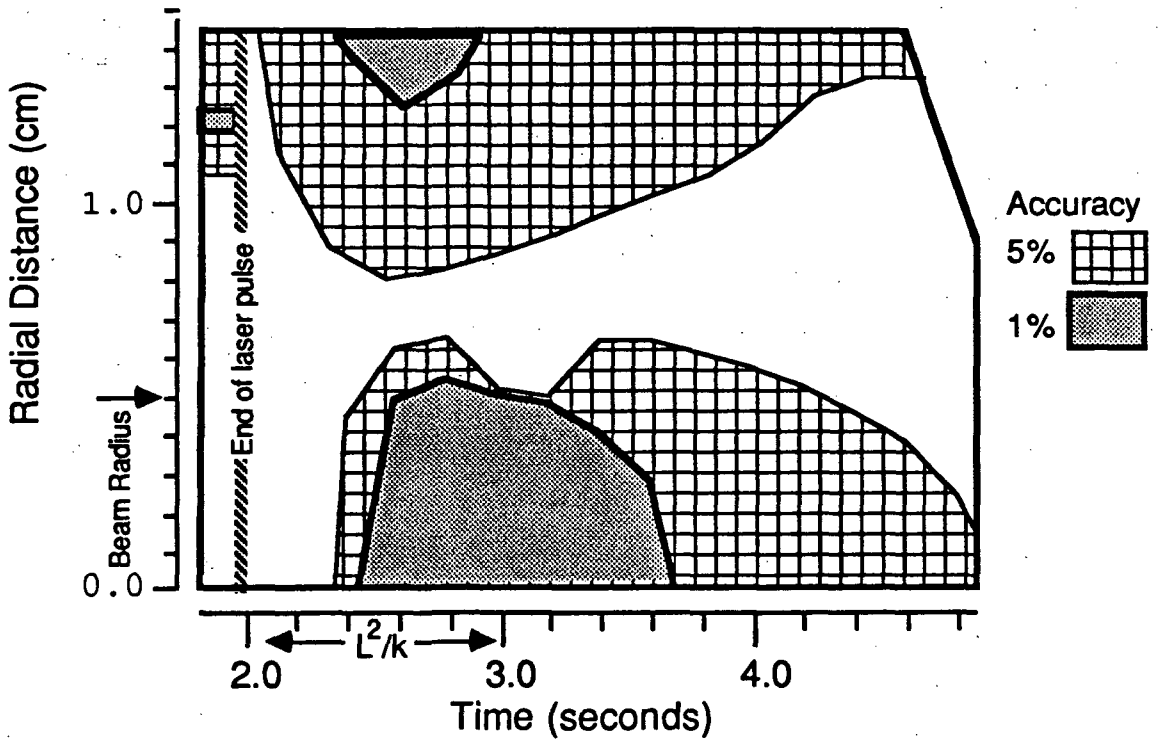

Figure 2.2. Model results showing regions of high and low accuracy for difffusivity calculations carried out with the primitive equation analysis on the surface of a homogeneous plate of finite thickness. The plate, with a diffusivity of .04 cm^2/s and a thickness of 2 mm represents the stainless steel laboratory samples. For this run, beam radius was 1 cm, pulse duration was 2 seconds, and power was 8 Watts. Peak temperature under these conditions at the end of the laser pulse reached 10.3 degrees C.

This run, although for only a single case, illustrates the behavior of the regions of both high and low accuracy. It is a plot of the accuracy of the diffusivity calculations as a function of both radial distance from the center

of the source and of time, and it includes all of the time for which good accuracy is obtained from the primitive equation method for diffusivity calculations. During the time that the laser is on, the diffusivity calculation gives accurate results in the far field, in corroboration with the analytic calculation. Immediately following the laser pulse, there is no region of accurate calculation. This corresponds to the L^2/k period during which the thermal pattern equilibrates through the thickness of the sample. Following this time, there appear two regions in which the calculations achieve accuracy of better than 1% separated by a band of inaccuracy. These will be called the near field and far field regions. The far field region recedes away from the source as time passes, while the near field is present for only a limited time. In the case presented, the width of the laser beam, 1 cm, is much greater tban the plate thickness, 2 mm. Other tests show that the width of the laser beam spot must be greater than the sample thickness for the near field to achieve high accuracy.

The qualitative behavior of the calculation can now be seen for the relationship between the distributed source case, which shows a limited region of high accuracy, and the point source solution, which shows only a far field region of high accuracy. During the heating time, the horizontal distribution of heat is largely determined by the source characteristics. In the far field, the temperature pattern is close to that expected from a point source of the same power, so the far field region of accuracy is established for the distributed case in the same way as for the point source. This region of high accuracy is likely to be of little use in NDE, because of small signal levels. Immediately following the source pulse, the heat flow is dominated by equilibration through the thickness of the plate, so the primitive equation method measures essentially irrelevant spatial derivatives, the result being low accuracy. In the time following this equilibration, which seems to be about half of the scale time (L^2/k), a high accuracy region is found to be located directly beneath the heat source. The radial limit of this region may be explained because, in an expanding heat spot, the center is cooling while the outer part of the pattern is heating. Thus, there is a location where the time derivative of temperature passes through zero. If the primitive equation calculation were perfect, the measured horizontal Laplacian would be zero at this same place. The numerator and denominator of the primitive equation thus both become zero in this region, so non-zero values from the calculation reflect entirely the small numerical inaccuracies in the model. With real data, they would reflect noise. At any rate, the calculation fails in a dead band around this zero time derivative region. As time increases, this dead band increases to the point where it eventually consumes the near field region of high accuracy. Subsequent to this, the accuracy of the solution resembles that found for the point source calculation. This corresponds to the concept that, at long times following a confined source pulse, the temperature from the pulse increasingly resembles that from a point impulse with equivalent total energy. In the case examined, the region of high accuracy persisted during a period between 0.5 and 1.5 times the scale time and within a radius equal to the acale redius of the source beam.

Based on the foregoing analysis, the answer to the original question can be expressed as a rule-of-thumb. To obtain good diffusivity estimates with the primitive equation method, the laser beam should be broadened to cover an area with diameter substantially larger than the thickness of the sample. This broadning need not preserve the Gaussian figure of a focused laser beam, but should have a central maximum and no "doughnuts" in the pattern. It should be directed at the sample for long enough to produce, following equilibration through the thickness, a good signal-to-noise ratio. If a scale time is defined as the ratio of the square of the nominal sample thickness to its nominal diffusivity, good accuracy in diffusivity measurements can be expected in the period from one-half to three-halves of the scale time in the portion of the sample under the heating pattern. If a nominal value of

diffusivity is not available, scale time can be estimated as the time for the original rapid temperature decrease following heating to occur under the central peak of the temperature pattern.

From a mathematical perspective, there is a behavioral similarity between the time variation of the diffusivity calculation and the accuracy of the asymptotic expansion for the exponential integral with an increasing number of terms [Morse, P. M. and H. Feshbach, Sec. 4.6]. If one considers the terms which are significant in the POINTEMP program, each one corresponds to a small source of heat located within the heated region on one of a set of image planes. Taken together, the sources are located within a bounded region at any given time, the bounded region having a shape like a stack of pancakes. At short times, few of the images are included in the sums, corresponding to just a few pancakes, the stack having mostly the shape of a single pancake. As time increases, more and more pancakes are added to the stack, which eventually resembles a long cylinder. At very long times, the cylinder resembles a string, the original shape of the pancakes becoming a relatively unimportant aspect of the total shape. The string corresponds to the shape of the analagous source region for the point source approximation. The accurate solutions are found within this progression during the time when the bounded region appears to contain several pancakes, or image planes, but before the time when it resembles a stack of coins. Thus, the region of accuracy for the diffusivity estimate does approach the correct diffusivity in an asymptotic manner, the approach reversing following some finite number of terms. In this sense, the two-dimensional model for thermal flow on a thin plate is seen to be an asymptotic approximation to the more realistic finite plate calculation.

2.4 Model Summary

The emphasis during the contract year shifted from examination of idealized models directed towards elucidating fundamental properties of thermal flow to models which can be compared directly with OPTITHIRMS data. The models constructed were all of the numerical integration type, forming sums of responses from patterns of idealized sources. Modifications to the formulation of the numerical equations were made to accommodate the singularity at zero radius. Model running time and computer environment were found to be significant new issues. To illustrate, two models which were constructed to produce temperature distributions from line scanned laser sources were found to have running times of 51 hours and 1.7 seconds, respectively. Besides providing correspondence with the available experimental data, the models were used to examine the correspondence between the two-dimensional idealization of a thin plate and its more realistic three-dimensional counterpart with respect to the primitive equation method for determining diffusivity.

3. Thermoelasticity

The thermoelastic effect is the thermodynamically associated change in temperature of an elastic material subjected to stress under adiabatic conditions. It is frequently ignored in elastic analyses because it represents a small part of the total stored energy in most common fabrication materials, and the temperature variations are quite small, on the order of hundredths of a degree. In contrast to the heat produced by material yielding, thermoelasticity is a reversible effect and is generally expressed as cooling under tension, rather than heating. Because the level of detection with the OPTITHIRMS system can be greatly increased under cyclic loading and because the thermoelastic effect produces, in principle, images which carry information about the stress distribution in an object under elastic cyclic loading, an investigation was initiated under this grant into the possible utility of thermoelastic image data for nondestructive evaluation of

graphite-epoxy composite structural members. In contrast with existing methods of examining stress distributions, thermoelastic variations detected radiometrically have the potential of providing image data, as opposed to collections of point data, with minimal disturbance of the object under test, for they sample only the thermal radiation which is emitted anyway by the object

The work under this phase of the contract was performed in collaboration with Sidney Allison of the Materials Characterization and Instrumentation Section of NASA Langley Research Center. He provided access to and operation of the MTS Stress-Strain machine in the section as well as a wealth of knowledge concerning mechanical testing techniques, sample clamping methods, and associated matters.

3.1 Literature Review

The first theory of thermoelasticity was formulated in 1855 by William Thomson (Lord Kelvin), and experimental verification was obtained to better than 0.1 percent in 1915 by Compton and Webster [Oliver, *et al*, 1982]. In oscillating motions, Zener [1938] applied the thermal conduction arising from thermoelastic temperature variations to the problem of damping of vibrations. Biot [1956] combined the thermomechanical and conductive equations to show that, when material deformation associated with temperature changes in conducting materials is taken into account, it is entropy rather than temperature which satisfies the diffusion equation. The actual use of infrared radiometry to examine structural stress was first reported by Belgen [1967a,b]. Another report of experiments relating stress to thermoelastic cooling was given by Heyman and Chern [1982]. Nayroles, *et al.* [1981] noted the existence of thermoelastic oscillations in infrared data taken to observe the propagation of a fatigue crack, and remove the thermoelastic signal as part of a search for the region of plastic deformation producing heating at the crack tip. Bouc, *et al.* [1983] reported the use of digitization of the infrared images obtained from a thermal imager to produce an image of the trace of the stress tensor around a crack tip. Oliver, *et al* [1982] reported the use of an infrared thermoelastic device which builds up images from a series of point measurements obtained through synchronous demodulation of signals with a stress-correlated driving signal associated with a sample under cyclic stress in its elastic regime. They made several comparisons between experimental results and theoretical solutions, both analytic and finite element, for the cases of a hole in a flat plate and a cylinder under compression. This work has led to the introduction of a product, the SPATE (Stress Pattern Analysis by Thermal Emission) 8000, a device which makes the synchronous detection approach to thermoelastic stress analysis commercially available.

The work reported above has been applied entirely to homogeneous materials, primarily metals. For this case and at temperatures well away from absolute zero, such as room temperatures commonly used in NDE, the temperature fluctuation under adiabatic conditions is directly proportional to the product of the ambient temperature and the sum of the principal stresses. The constant of proportionality is the ratio of the linear thermal expansion coefficient to the volumetric heat capacity at constant pressure, and the sign is chosen so that tension produces cooling. These relations are expressed as

$$\theta = -K_M T \sigma \tag{3.1}$$

with

$$K_M = \alpha_x / c_p. \tag{3.2}$$

Here θ is the amplitude of the temperature fluctuation, σ is the amplitude of the sum of the principal stresses, and T is the absolute value of the ambient

temperature. K_M is called the thermoelastic coefficient, and it is a property characteristic of any given material. α_x is the linear coefficient of thermal expansion, and c_p is the volumetric heat capacity at constant pressure. Belgen [1967b] notes that the actual temperature fluctuation is different at high stresses, which are frequently used to obtain large signal values in samples, because the pressure within the sample varies with the strain during each cycle, and so c_p is not the appropriate value, but rather an intermediate value between c_p and c_v.

It is not immediately clear how this formula should be altered for the case of non-isotropic materials, for the temperature fluctuations evidently come about through an interaction of the strains with the thermal expansion terms. In an anisotropic material, both are represented by second order tensors, and the appropriate interactions are not intuitively clear.

3.2 Experimental Work

The experimental work has been carried out in facilities made available through the Materials Characterization Information Section (MCIS) of NASA Langley Research Center. The particular experimental configuration consisted of an MTS fatigue stress machine, rated at 110 thousand pounds, the VAX 750

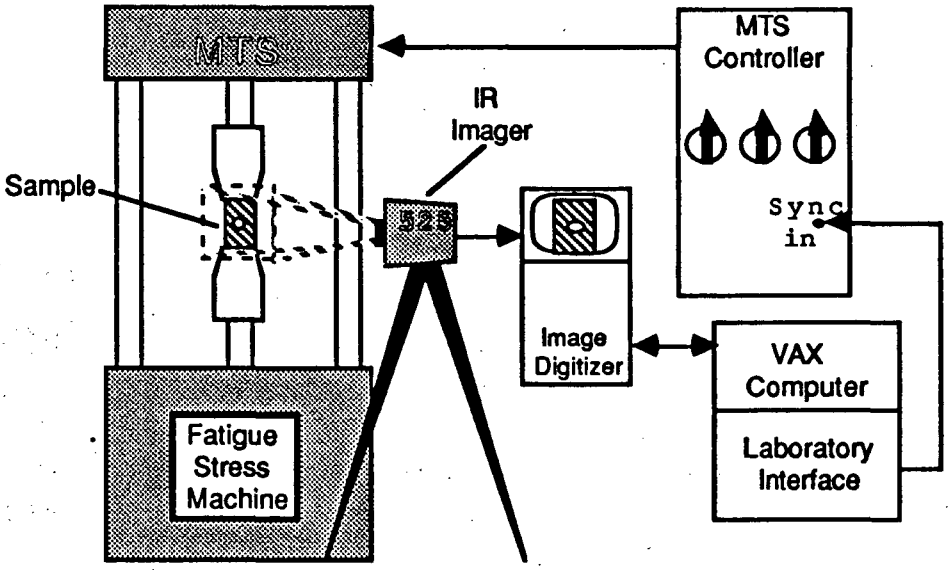

Figure 3.1. Experimental configuration for thermoelastic measurements.

computer associated with MCIS, and an Inframetrics Model 525 Infrared Imager. The VAX is attached to a Grinnell image processing system with a video digitizer and to an LPA-11 laboratory interface, which is used as a synchronization pulse generator. The experimental configuration is shown in Figure 3.1.

In operation, the imager generates the video synchronization signal, which cycles 30 times per second and is not synchronized with the remainder of the system. The MTS machine is set up with a single cycle ramped pulse initiated from an external synchronization pulse. The ramp times, hold time, and maximum load level are set with panel controls on the MTS controller. The VAX, under the program MTS_Control (Appendix 1), initiates a data cycle by instructing the Grinnell digitizer to obtain a positive image and add it to its image buffer. After a user-chosen delay, the VAX instructs the Laboratory

Interface to send the synchronization pulse to the MTS machine. The computer also sends, following the synchronization pulse by a user-chosen interval, another instruction to the image processor to digitize a negative image and add it to the image buffer The cycle is repeated after a settling time subsequent to the second image. The cycle timing diagram is shown in Figure 3.2. In addition to running the data cycle, MTS_Control initializes the

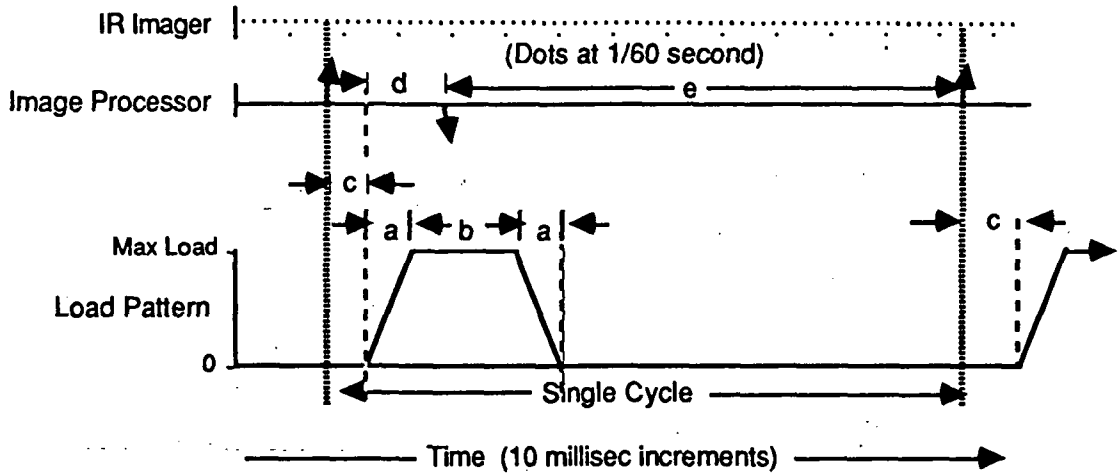

Figure 3.2. Thermoelastic cycle timing and control. Max load, ramp time (a) and hold time (b) are selected on the MTS Fatigue Loading Machine. The cycle starts with the instruction to acquire a positive image, which is actually obtained at the next imager frame cycle (2/60 sec) subsequent to the command. The MTS cycle is initiated after a synchronization time (c) following the cycle start. The negative image is obtained at the first frame time following a time interval (d) from the sync pulse, and the cycle is repeated after a settling time (e) following the negative image. Cycle time is the sum of (c),(d) and (e).

Grinnell by setting its image buffer to an intermediate value and halts following a user-chosen number of cycles, saving the final image in a disk file with a user-chosen name. Later versions of the program also transfer the contents of the Grinnell image buffer to a summing buffer in the VAX following a small number of cycles, also user-chosen. The reason for the transfer is that the image buffer sums and stores quickly, in a frame time, but has limited dynamic range. The computer memory has very large dynamic range, but transfer from the Grinnell requires 9 seconds per image. The sub-sampling scheme is chosen to provide the large dynamic range of the computer buffer to the data while incurring a minimum time penalty from the data transfer operation. To increase the effective dynamic range at the expense of resolution, the program also shifts the incoming data down one bit following digitization and prior to summation. The low order bit from the 8 bit digitizer (1 part in 256) contains little information when the camera noise level is .15 degrees in 10 (3.8 parts in 256), so its loss is of little significance.

On the advice of the technical staff of the Materials Division of NASA Langley Research Center, who are thoroughly versed instress distribution, the equipment was used to examine a sample consisting of a metal plate with a circular hole in the center, as a close approximation to a situation with plane stress distribution around a hole in an infinite plate subject to uniform unidirectional stress at large distances away from the hole. This case, besides applying to holes used for fastening sheet metal, is experimentally convenient because the sum of the principal stresses is described by a simple function which is localized around the hole and attains

both positive and negative values

$$\sigma = \sigma_{\infty}\left[1 - 2\left(\frac{R}{r}\right)^{2}\cos\ (2\theta)\ \right]. \qquad (3.3)$$

Here, R is the radius of the hole, the formula applying only outside this radius, θ is the angle of a polar coordinate system with zero angle in the direction of far field stress, denoted as σ_{∞}, r is the radial coordinate for the polar system, and σ is the sum of the principal stresses.

The experiment to examine the system response compared with the ideal response was performed on a plate of Type 347 stainless steel 2.95 mm in thickness. Stainless steel was chosen because its relatively small value of thermal diffusivity reduced the evolution of the temperature field due to thermal conduction during the period of production and acquisition of experimental data. Thus, the adiabatic approximation was experimentally valid. The plate was 102 mm wide and 629 mm long with a hole 19.0 mm in diameter placed in its center. Its central portion was coated with a high emissivity coating to produce high-efficiency emission in the infra-red. The plate, which was self-aligning in the MTS machine owing to its width in the hydraulic grips, was cycled for 20 times at a maximum load of 5,000 pounds. The load cycle had ramp times of 50 ms and a hold time of 100 ms. The cycle repeat time was 990 ms. Image acquisition instructions were issued at cycle times zero and 200 ms. The images obtained were saved, and the experiment repeated 5 times. As four of the five realizations looked qualitatively similar in the resulting stress images, their sum, containing a total of 80 stress image pairs, was used to form a stress image with random noise reduced by a factor of 8.9 over a single image pair. The fifth realization was rejected because of a qualitative judgement that image "banding" due to instrumental noise was too great.

The image data were further processed to obtain the temperature deviation profiles along the principal axes of the plate, and the data are shown compared to theoretical values in Figure 3.3. The two pairs of data/model curves are taken from the image data along the two principal axes of the experiment, through the hole along the center line of the plate and across the plate perpendicular to the center line and through the center of the hole. To reduce noise, the data were first filtered by averaging over a 4 by 4 pixel area from the video image. The resulting average values each cover an area equal to about two independent points of infrared data, the translation scheme used to obtain video formatting being highly redundant. In forming the data lines, the samples are further averaged over four parallel lines nearest to the principal axes, the lateral variation being small in these regions.

The theoretical values used in Figure 3.3 were taken from equation 3.3 and modified using a filter to describe the sampling area of a single image. The filter was a running average (a "boxcar" filter) encompassing the points within a given segment length of the model. The segment length is chosen to match the slope obtained in passing the filter over the edge of the hole with that observed in the data, under the assumption that the radiation field at the edge of the hole approaches a step function as closely as possible.

The fit of the experiment to the model in figure 3.3 is qualitatively good, indicating that the temperature variations observed in the data are due, as anticipated, to the thermoelastic effect. Of particular interest is that the area of net compression predicted from the theory corresponds to the observed temperature rise in the same region. The data thus exhibit temperature fluctuations in the same general pattern as those expected from thermoelastic theory and have signs indicating both heating and cooling, consistent with thermoelasticity and inconsistent with dissipative

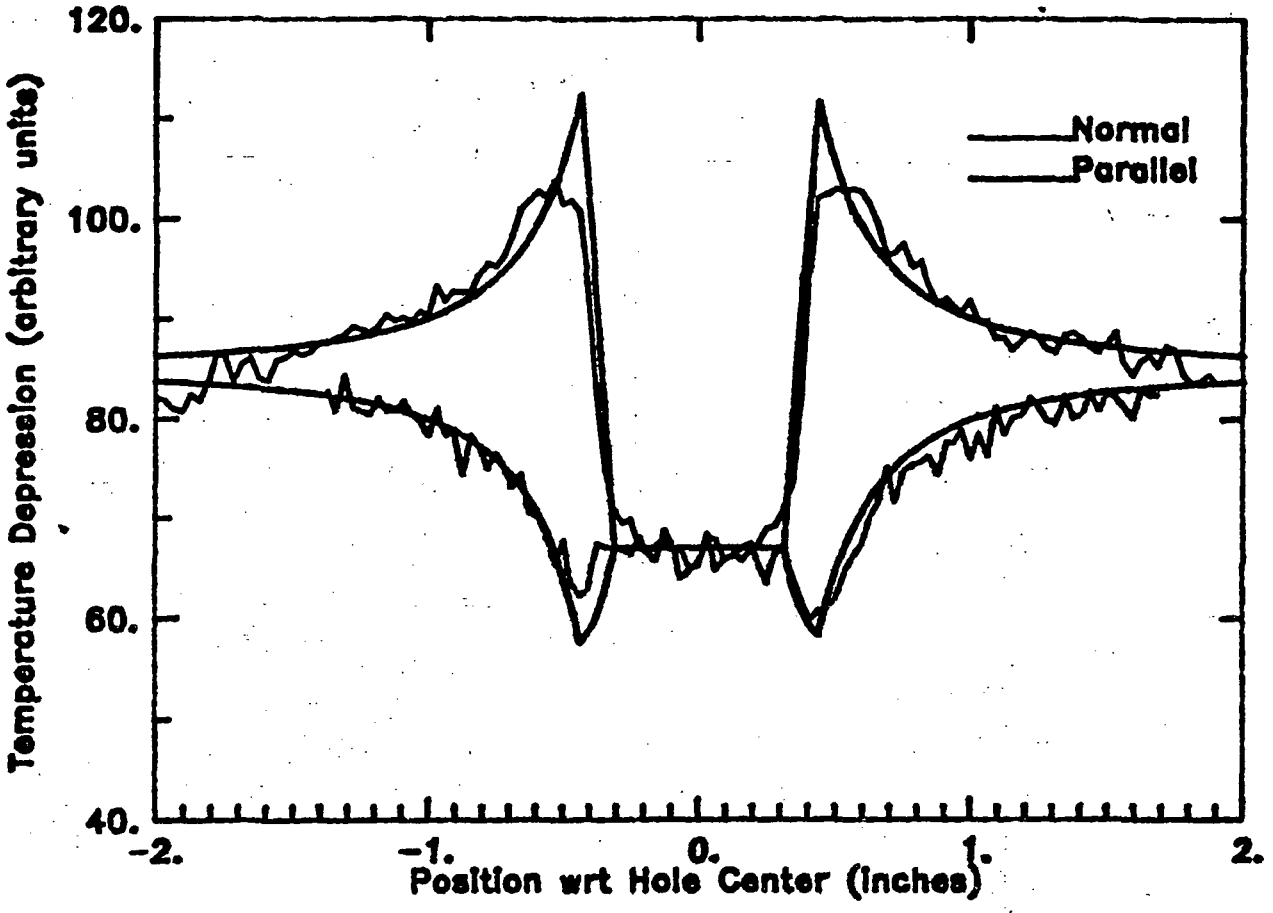

Figure 3.3. Comparison between thermoelastic data and model. Fitting parameters include 67 vertical units for the temperature depression within the hole, the zero value; 85 vertical units for the temperature depression corresponding to unit stress; and .12 inches for the detector "footprint" size. Comparisons for both along-sample and across-sample axes are shown, with the observations showing the effects of instrumental noise.

heat-producing effects, the other candidates for producing temperature contrast in the image.

There are aspects of the data which invite further interpretation and analysis, however, as they are to a greater or lesser extent questionable or paradoxical. The stress pattern extending across the plate dips down at the edges of the plate (at plus and minus 2 inches) on both edges. This suggests some kind of edge effect which may be of interest or may reflect some experimental factor not presently included. The size of the boxcar window required for a close fit to the data came to about .12 inches, or 1/32 of the field of view. This contrasts with the 0.04 inches expected from the manufacturer's specification for the number of independent values in a line. Another estimate of the resolution may be obtained from a comparison of expected and observed noise levels. The expected noise level is calculated to be 2.15 Grinnell units (the scale used for temperature in Figure 3.3), while an analysis of the noise observed in one of the frames used in producing Figure 3.3 gives a standard deviation of 3.5 units. The expected noise value is based on the value of 100 independent samples in the horizontal field of view. If this factor is increased to a value consistent with 32 independent values per line ($\sqrt{(100/32)}$), the expected noise becomes 3.8 units, quite close to the observed 3.5 units. Thus, it appears that the horizontal resolution of the imager in this data was less than the manufacturer's suggested value by a

factor of 3. The difference may be due to the employment of the electronic zoom feature of the imager to fit the video image into the full video frame, thereby enlarging the portion of the image occupied by the electronic footprint. Other possibilities are poor focusing in the data or vibration of the imager relative to the sample. Since the noise analysis and the step function analysis produce similar values for system resolution, it seems appropriate to investigate the system resolution directly in a continuation of this work.

In another comparison, the value of the vertical axis corresponding to the far-field stress used in the model is 18 of the Grinnell units. An expected value can be calculated from handbook values of thermal expansion coefficient, heat capacity and density, using equations 3.1 and 3.2. The expected value is 18.8 of the Grinnell units. Given the uncertainty in determination of the model parameters, estimated at 2 Grinnell units, the agreement here is excellent.

Finally, the figure of the experimental curve is more "rounded" on the top of the experimental data than on the bottom. One effect of this rounding is that the peak value of the observed data, corresponding to the point of maximum stress, misses the expected value by the greatest amount of any part of the image. This is of concern because it is this value, the greatest stress in the pattern, which is of greatest interest in much engineering stress analysis. In addition, the data lie consistently above the model in the region of the top curve outside of the rounded top. The roundedness of the top with associated the vertical offset further out are of some interest, as one of the possible explanations is that the sample was taken slightly beyond the elastic limit with the 5000 pounds of force applied. With the cross section of .5 square inches, the far field stress is 10,000 pounds per square inch (10 Kips). The "stress factor" for the infinite geometry is 3.00, where stress factor is the standard engineering term for the ratio of maximum stress to the far-field stress. When the first standard correction for width is taken into account, the stress factor for our plate is 3.13, resulting in a stress of 31.3 Kips for our configuration. When the finite width is taken further into account, the stress factor in the center plane of the plate is slightly larger than this value. The handbook value for 0.2% yield for the sample material is 35 Kips. Given the closeness of the experimental stress to the 0.2% yield value, the character of the yield curve for Type 327 Stainless Steel, which is gradual, and the possibility that the experimental protocol may cause a little overshoot in the MTS machine, it is not unreasonable to consider that the high stress portions of the samplemay have yielded slightly. Measurements of the thickness of the inside of the hole revealed less than .001 inches of thinning, the limit of the measurement, but the expected yield would draw the material less than this amount. Because the sample had been subjected to more than 150 cycles of stresses at the 5000 pound level (but none at higherloads), the signal from initial yielding is not included in the analyzed data. The evidence for yielding would be present in the sample only as a residual stress.

Under the experimental protocol, the sample was subjected to multiple cycles of stress and relaxation, the stress level being uniform for each cycle. The yielding would occur, and produce heating, during the first of the multiple cycles, but not on following cycles. Following the first cycle, the yielding would leave a pattern of residual stress, which would be sufficient, along with the work hardening, to halt the strain on the subsequent cycles just prior to the yield point. In conversations with analysts, it appears that the strain pattern subsequent to the yielding would be different from that without yielding, and that the resulting alterations in the strain pattern would qualitatively resemble those in the observations. It is thus plausible that the rounding of the upper peak in the data is the result of residual stresses in the sample due to yielding during the experimental setup.

The detection of residual stress or evidence of prior excedence of the

elastic limit is of interest in many potential applications of non-destructive testing. It is recommended that the experiment reported here be continued by subjecting a sample similar to the one examined here to multiple cycles at increasing stress levels to see if the rounding pattern occurs subsequent to, but not prior to yielding and to examine its evolution as the load is increased to produce more severe yielding.

3.3 Application to Composite Materials

Samples of impacted composite material have been placed in the apparatus and examined both with our imaging system and with an Ometron Spate 8000. The direct result is that the thermoelastic signal is much smaller than in steel samples and that direct contrast around the impact damage is not much larger than that in the region not subject to impact. On the other hand, when an examination of the region centered on the impact point is made, the thermoelastic signal does seem to change qualitatively in its character compared to an unimpacted region. Thus, the utility of thermoelasticity to detect impact damage in composite materials is neither immediately established nor clearly disproven. To examine the question further, it is necessary to look further into the nature of thermoelasticity in graphite-epoxy composite materials.

At the most primitive level, considering only the bulk properties of the materials, many of the fabrication patterns for graphite-epoxy are designed to have a very small, essentially zero, coefficient of thermal expansion. This coefficient is in the numerator of the expression for the thermoelastic coefficient, so a zero value implies that there will be no thermoelastic temperature response to stress. This provides some insight into the small levels of thermoelastic signal observed in graphite-epoxy samples. The signals are not zero, however, and patterns of contrast are seen in experimental data.

At the next level of complexity, a graphite-epoxy material may be considered to be a composite of two materials, graphite fibers embedded in an epoxy resin matrix. The graphite fibers are highly anisotropic, having very high strength and modulus of elasticity in their long direction. Their coefficient of thermal expansion in the along-fiber direction is actually slightly negative at room temperatures. In the cross-fiber direction, their coefficient of thermal expansion is actually fairly large and positive. On heating, then, there is a net volume expansion of a graphite fiber in such a way that it becomes slightly shorter and a lot fatter. In contrast, the epoxy resin matrix is relatively isotropic, weak, and even compressible, with a fairly large coefficient of thermal expansion. If one considers the transmission of stress along the fiber direction in a composite material made of these two components, the majority of the load in a section is carried by normally stressed fibers, while the matrix transfers load between adjacent fibers through shear stresses at relatively low levels. The thermoelastic effect is associated in isotropic materials only with normal stresses. The thermoelastic effect from the fibers is thus zero, as their coefficient of thermal expansion in the load direction is zero, and that from the matrix is also zero, as it is loaded in shear. One can envision loading a composite material at an angle to its primary axis and producing normal stresses in the matrix material, which then give rise to thermoelastic signals. With this perspective, it may be that the generation of thermoelastic signals which are observed in composite samples is related to non-uniformities in the distribution of stress within the material which lead to patterns of normal stress in the matrix. Observation of such non-uniformities may be of interest in NDE and process control.

Two further factors need to be considered before the observed patterns can be related to material flaws. The observed signals come primarily from temperature changes generated at the surface of the material, with the

associated contrast transmitted to the surface layer by means of the stress distribution. The signals arise only secondarily from temperature anomalies generated within the bulk of the material and transmitted to the surface by thermal conduction. These two paths of transmission may be discriminated through the delay of the thermal conduction signal relative to the stress-transmitted signal. To the extent that the observed signal is produced to the dilitation of the surface layer, techniques other than thermoelasticity, involving special surface coatings which are brittle or change optical properties in response to strains, may provide superior NDE probes. The other factor is that the theory presented here is based on isotropic materials while the graphite fiber component of the composite is notably anisotropic. In order to obtain an independent estimate of the thermoelastic temperature from the graphite component of the composite, the thermoelastic theory for non-isotropic materials must be found or derived and applied to graphite fibers.

It is recommended that further research into the application of thermoelasticity to the NDE of graphite-epoxy composite materials take the path of describing the source of the observed signals. From the present, incomplete, perspective, it appears that the signals obtained from thermoelastic measurements arise from non-uniformities in the distribution of strain within a material rather than as characteristics of the normal state of the material subjected to cyclic stress.

References

Abramowitz, M. and I. A. Stegun, eds.,1965, Handbook of Mathematical Functions, Dover Publications, Inc., New York, 1046 pp.

Belgen, M.H., 1967a, Structural Stress Measurements with an Infrared Radiometer, ISA Trans. 6(1), pp. 49-53.

Belgen, M. H. 1967b, Infrared radiometric stress instrumentation application range study, NASA CR-1067, 142 pp.

Biot, M. A., 1956, Thermoelasticity and Irreversible Thermodynamics, J. Appl. Phys. 27(3), pp 240-253.

Bouc, R., P. Bremond and P. Nayroles, 1983, Numérisation du signal vidéo et analyses des contraintes par thermographie infrarouge, C. R. Acad. Sc. Paris, Série II 296,pp. 673-676.

Carslaw, H. S. and J. C. Jaeger, 1959, Conduction of Heat in Solids, Oxford University Press, Oxford, U.K., 478 pp.

Gradshteyn, I. S. and I. M. Ryzhik, 1980, Table of Integrals, Series, and Products, Translated and edited by Alan Jeffrey, Academic Press, New York, 1153 pp.

Heyman, J. S. and E. J. Chern, 1982, Ultrasonic measurements of axial stress, J. Testing and Evaluation 10(5), pp. 202-211.

Lax, M, 1977, Temperature rise induced by a laser beam, J. Appl.Physics 48(9), 3919-3924.

Morse, P. M. and H. Feshbach, 1953, Methods of Theoretical Physics, McGraw-Hill Book Company, New York, 1978 pp.

Nayroles, B. R. Bouc, H. Caumon and J. C. Chezaux, 1981, Téléthermographie Infrarouge et Mécanique des Structures, Int. J. Engng. Sci. 19, pp. 929-947.

Oliver, D. E., D. Razdan and M. T. White, 1982, Structural design assessment using thermoelastic stress analysis (TSA), British Society for Strain Measurement/Royal Aeronautical Society Joint Conference "'State of the art' in Measurement Techniques", University of Surrey, 6-9 September, 23pp.

Zener, C., 1938, Internal friction in solids: II, General Theory of Thermoelastic Internal Friction, Phys. Rev. 53, pp 90-99.

Appendix 1

Summary of Computer Programs

Thermal Models

POINTEMP.FOR - This program uses a Green's Function analysis to compute the surface temperature as a function to radius and time due to a Gaussian flux of heat absorbed on the surface of a thin plate over a finite length of time at a uniform rate. Zero heat loss is assumed at the front and back face of the plate. Physical and control variables are stored in two separate files COMTROL.FOR and PHYSICS.FOR. The function routine ERFC is called to produce values for complementary error functions used in the calculation. The resulting tables, stored in an array called POINTPLOT.DTA can be expressed in a form compatible with the plotting package IAP with program POINTPLOT.FOR. Further calculations of estimates for spatial and temporal derivatives used for estimating diffusivity by the primitive equation method (see text) are done on the POINTOUT.DTA files with the program CALCK.FOR and placed in another file called DIFFEST.DTA. Physical parameters, temporal increments and limits, pulse durations and radial scale, and radial increments and limits are all chosen by the user.

LTEMP.FOR - This file contains one of the masters for program LINETEMP. This program uses Green's function analysis to produce the estimated thermal pattern at a given time due to a Gaussian laser source which is scanned in a straight line over the face of a semi-infinite (very thick) material. The version stored in LTEMP.FOR produces the estimate for an image with 480 lines each with 512 pixels. The version stored in SMLLTEMP.FOR uses an image of 120 lines and 128 pixels. The smaller version was found to run much faster than the larger one (see text) and is recommended for use. File references and parameter values are stored in files FILE.FOR and PARAM.FOR, with values obtained in subroutines GETFILES.FOR and GETPARAMS.FOR. (For SMLLTEMP, GETPARAMS.FOR is replaced with LPARAM.FOR.) Calculation boundaries are calculated in subroutine BOUND.FOR, and calculation of laser (heat pulse) intensity is done in subroutine PS.FOR. Pulse parameters that are user-specified include power, line position, line length, line scale width, line orientation, and pulse length. Material properties include thermal conductivity, heat capacity, and surface emissivity. Image parameters include pixel size and image time. The output is in a form that can be translated into the form used in the image processing package SADIE.

TLINE.FOR is a subroutine that calculates the temperature in a thin plate of homogeneous material subsequent to an initial temperature which represents the cross-section of a linear temperature pattern extending through the thickness of the material. It uses an evaluation of Laplaces solution to the one-dimensional heat equation (see text). The subroutine calls the function ERFC.FOR to evaluate the value for the complementary error function.

LINEVFY.FOR is a program which calls TLINE and uses it in an initialization-prediction mode to compare with data from actual experiments. The routine contains two user-chosen parameters, the thermal diffusivity of the material and a heat loss factor, corresponding

to the rate of fractional heat loss from the sample through processes of radiation and convection. Experimental data is retrieved from files written in the "9 line format" by subroutine GET_TEMP_DATA, supplied by W. Winfree. The program uses the first line of the 9 experimental lines as initialization and producesdata, model and difference lines in a form directly compatible with the plotting package IAP. In doing its comparison, it removes a baseline value for each data line baaed on the average of 50 values (out of 256) from each end, calculates the total heat at each time, calculates the total variance as a function of time, and passes the time data through to an IAP file.

RATIO.FOR - This program evaluated the thermal pattern due to a point source (see text) on a thin but finite plate and showed that the primitive equation diffusivity calculation produced no region of asymptotically correct values in the vicinity of the source.

Thermoelasticity Programs

MTS.FOR - This program, written by A. Dail, controls the experimental timing between the VAX computer, the Grinnell Image Processor and the LPA-11 laboratory interface to execute a thermoelastic experiment. Many of the experimental parameters (see text) are chosen by the user for each experiment. It saves the resulting image file in a user-defined file, which can be changed into a format compatible with the image analysis package SADIE with program SADDAT, written by J. Moore.

MOD.FOR - This program calculates model values for thermoelastic temperature fields along the central transverse line across a plate with a hole in it (see text). It filters the data with a boxcar filter to simulate the effect of a finite "footprint" for the active detector area.

FIT.FOR - This program compares the calculations from a model to the data at the same set of position coordinates and calculates the variance of the residual.

Miscellaneous and Utility Programs

DISPLAY.FOR - This program, written by A. Dail, displays data in an image file format on the Grinnell Digitizer viedo output.

TEMPDIS.FOR - This program, written by A. Dail, displays a user-chosen "window" of data in an image file format as a pair of hexidecimal digits on the screen of a terminal. It is used for low-level tracking of numbers through the video imaging process.

ERFC.FOR - This function subroutine provides a fast calculation of complementary error function used in many thermal models. It is extended analytically to provide symmetric values for negative values of the argument as erfc(-x) = 2.0 - erfc(x).

BIFR.FOR - This is a routine for the I Bessel Function (Modified Bessel Function of the First Kind) which was imported from the NASA Central Computer Facility and changed to operate on the VAX.

Appendix 2

Translation of "Infrared Thermography and Structural Mechanics"

During the literature review, the paper "Téléthermographie infrarouge et mécanique des structures" by B. Nayroles, et al. was discovered describing French work which is closely related to our work both in approach and in purpose. To provide this information to the team within MCIS, the paper was translated into English as part of the effort under this contract. The translation follows.

INFRARED THERMOGRAPHY AND STRUCTURAL MECHANICS

by

B. Nayroles, R. Bouc, H. Caumon and J. C. Chezeaux
C.N.R.S Laboratory of Mechanics and Acoustics, Structural Radiation Group,
31 Joseph-Aiguier Rd., BP 71, 13277, Marseille Cedex 9, France.

and

E. Giacometti
National Society for Aerospace Industry, (S.N.I.A.S) Helicopter Service,
Marignane, France

Abstract

Possible applications of recent IR movie systems are looked at in the field of structural mechanics. Two main phenomena are involved, on the one hand, the isentropic temperature variations which occur during a periodic evolution, on the other hand, the dissipation of mechanical energy. After some elementary recalls of thermodynamics, some details are given concerning the accuracies which are available when a suitable signal processing is undertaken or not. Finally the largest developments seem to be possible in the next years.

1. INTRODUCTION

For several years, infrared cameras, which provide visual images of temperature variations less than 0.2°C around ambient, have been commercially available. Whatever the method of detection, a photo-sensitive cell or a pyroelectric detector, these instruments deliver an analog picture signal and synchronization signals which allow reconstruction of an image obtained by scanning: the standard configuations provide information which can produce immediate visual images, if attached to displays, or optionally may be digitized. In fact, the most recent uses are instantaneous visual inspection of heat flow in buildings, overheating in electrical circuits, or other thermal anomalies, such as those due to subcutaneous tumors. It is remarkable the substantial industrial and medical market already open for these devices while their laboratory use remains quite limited.

It is natural to inquire what applications these devices might have in the Mechanics of Solids, either in their present state or with improvements attainable through numerical processing. This is the type of question we propose to answer in this article along with presentation of results already obtained in our laboratory and those of S.N.I.A.S, with which we have been associated for a large portion of these studies.

While the literature is generally sparce, we cite works of particular interest from fracture mechanics [1,2], non-destructive testing [3-5], vibration mechanics [6] and plastic deformation [7]. Finally, in an article to appear [8,9], an experimental study of the thermomechanical behavior of materials is considered using stroboscopy of IR thermography. First, we consider the source of heat caused by dissipation of mechanical energy: that due to internal friction present within the structure or that due to plastic deformation. Nevertheless, the reader should realize that the experiments described are only feasability demonstrations, a large number of physical

parameters having not been measured or determined with the requisite preparation. In contrast, a substantial experimental program is planned for the near future to compare experiment with theory for dissipation mechanisms at a crack tip (Nguyen Quoc Son [10])

We will see that the application of infrared thermography to structural mechanics is restricted because of the limited precision available in the standard commercially available models. On the other hand, digitization of the signal, summation of the images and the resulting improvement in signal-to-noise ratio permits considerations such that, with such accuracy as well as speed of operation or ease of use, IR thermography should gain an important place in structural mechanics laboratories.

2. PHENOMENA OF THERMOMECHANICAL STUDIES

2.1 Review of the three-dimensional equations of thermomechanics

We consider a three-dimensional solid which occupies a volume Ω in space with its exterior surface denoted by $d\Omega$. Under the hypothesis of infititesimal geometric displacements, one obtains the relation

$$\varepsilon_{ij} = (1/2)(u_{i,j} + u_{j,i}) \tag{1}$$

where ε designates the deformation tensor and $\mathbf{u}$ the vector displacement.

We make the general hypothesis that the various energy variables are distributed, *i.e.* they can be represented by volume densities as follows: ρ, mass density; $(1/2)\rho\dot{u}^2$, kinetic energy density, U, internal energy density; W, Helmholz Free Energy density; S, entropy density; D, density of power dissipation.

Further, we suppose that at all points M within Ω, the Helmholz Free Energy, W, is a function of the deformation, ε, the absolute temperature, T, and "internal variables." The formalism used here is applicable, without particular limitations, provided the internal variables are the components of a variable, η, which can be expressed in a vector space of finite dimension. To illustrate, one may consider η to be a tensor of the same type as ε. This implies, in summary,

$$W = W(x, \varepsilon, \eta, T).$$

Furthermore, by the definition of W

$$\sigma = \frac{\partial W}{\partial \varepsilon}, \; S = -\frac{\partial W}{\partial T}, \; U = W + TS \tag{2}$$

where σ denotes the stress tensor.

Designate respectively by P_{MEC} and P_{CAL} the mechanical and thermal power supplied to the solid by its surroundings.

The First Law of Thermodynamics is written

$$\int_{\Omega} (\dot{U} + \rho \dot{u}\dot{\bar{u}})\, d\Omega = P_{MEC} + P_{CAL} \tag{3}$$

while the Second Law is written

$$P_{CAL} \leq \int_{\Omega} (T\dot{S} - D)\, d\Omega, \quad D \geq 0 \tag{4}$$

Moreover, the mechanical energy balance is

$$\int_\Omega \rho \dot{u} \tilde{u} \, d\Omega = P_{MEC} - \int_\Omega \sigma \cdot \dot{\varepsilon} \, d\Omega \qquad (5)$$

Substituting in (3) P_{CAL} and P_{MEC} by their expressions in (4) and (5) and using relations (2) to expand U, one obtains conventionally,

$$D = -\frac{\partial W}{\partial \eta} \cdot \dot{\eta} \qquad (6)$$

Next, denote by $\mathbf{q}$ the vector flux of heat within the solid, and assume the linear law of Fourier

$$\mathbf{q} = - k \cdot \text{grad } T \qquad (7)$$

where k is the tensor of heat conduction. Denote by ϕ the volume density of any possible sources of heat within Ω; we can express

$$P_{CAL} = - \int_{\partial\Omega} \hat{n} \cdot \mathbf{q} \, d(\partial\Omega) + \int_\Omega \phi \, d\Omega$$

where $\hat{n}$ designates the unit outward normal vector. The divergence theorem gives

$$P_{CAL} = \int_\Omega (\phi - \text{div } \mathbf{q}) \, d\Omega \qquad (8)$$

On replacing P_{CAL} by its expression in (4), and seeing that the relation should apply to all sub-volumes of Ω, one obtains the local relation

$$\phi + \text{div}(k \cdot \text{grad } T) = T\dot{S} - D.$$

Now, calculating $\dot{S}$ from the second of equations (2) produces

$$\phi + \text{div}(k \cdot \text{grad } T) = -T \left(\frac{\partial^2 W}{\partial T \partial \varepsilon} \cdot \dot{\varepsilon} + \frac{\partial^2 W}{\partial T \partial \eta} \cdot \dot{\eta} + \frac{\partial^2 W}{\partial T^2} \dot{T} \right) \qquad (9)$$

On the right-hand side, the tensor quantities

$$l = -\frac{\partial^2 W}{\partial T \partial \varepsilon}, \quad m = -\frac{\partial^2 W}{\partial T \partial \eta}$$

are the thermoelastic coefficients, while the scalar

$$c_{\varepsilon,\eta} = -T \frac{\partial^2 W}{\partial T^2}$$

is the volumetric specific heat with ε and η constant.

With these notations, the heat equation is written

$$c_{\varepsilon,\eta} \dot{T} = \text{div}(k \cdot \text{grad } T) - (l \cdot \dot{\varepsilon} + m \cdot \dot{\eta}) T + \phi + D. \qquad (10)$$

Examination of the right-hand side reveals that temperature changes are due to three types of causes:

1. Conduction, represented by the first term, which tends to make the field uniform

2. Reversible effects, represented by $(l \cdot \dot{\varepsilon} + m \cdot \dot{\eta})$; when conduction, dissipation and internal sources can be neglected, the temperature varies with a linear combination of apparent and hidden deformations; the coefficients l and m are small, but the sensitivity of existing cameras permits observations of these variations.

3. Heat sources, with which the dissipation of mechanical energy may be grouped.

It is the reversible terms and the dissipation which we wish to evaluate from measurements of the temperature field made by an IR camera.

With equation (10) is associated the equation of motion,

$$\rho\ddot{u} + \operatorname{div}\sigma = f, \tag{11}$$

the geometric relation(1) and the equation of state, symbolically

$$\sigma = \boldsymbol{F}(\varepsilon, T) \tag{12}$$

where the functional $\boldsymbol{F}$ is in fact defined by a differential system depending on σ, ε, η and T. We note that the derivative of the first of relations (2) gives

$$\dot{\sigma} = \frac{\partial^2 W}{\partial\varepsilon\partial\varepsilon}\cdot\dot{\varepsilon} + \frac{\partial^2 W}{\partial\varepsilon\partial\eta}\cdot\dot{\eta} - 1\dot{T}. \tag{13}$$

To illustrate the developments which follow, we present two examples which are simple as well as highly useful in practice

Eaample 1: Linear Viscoelasticity

We consider a substance whose mechanical behavior is represented by the following rheological model (Fig. 1). The upper portion represents the thermal dilitation $e^0(T)$. Define the tensors of stiffness and the viscosity K^1, K^2 and V, considered independent of temperature, and the specific heat at constant stress, C, which are relatively easily determined experimentally.

The equations of mechanics are

$$\sigma = K^2\cdot[\varepsilon - \eta - e^0(T)] = K^1\cdot\eta + V\cdot\dot{\eta}.$$

From the first and the obvious expression

$$D = \dot{\eta}\cdot V\cdot\dot{\eta}$$

one infers that the form of the Helmholz Free Energy is

$$W = \tfrac{1}{2}[\varepsilon - \eta - e^0(T)]\cdot K^2\cdot[\varepsilon - \eta - e^0(T)] + \tfrac{1}{2}\eta\cdot K^1\cdot\eta + f(T) \tag{14}$$

where the function f remains to be determined. At zero strain, ε is reduced to $\dot{e}^0$, and (10) reduces, assuming $f = cT$ and grad $T = 0$, to

$$c_{\varepsilon,\eta}\dot{T} = -Tl\cdot\frac{de^0}{dT}\dot{T} + c\dot{T}$$

since from (13) one infers

$$l = -m = K^2\cdot\frac{de^0}{dT} \tag{15}$$

it leads to

$$c = c_{\varepsilon,\eta} + T\frac{de^0}{dT}\cdot K^2\cdot\frac{de^0}{dT} = -Tf''$$

and finally

$$W = \tfrac{1}{2}[\varepsilon - \eta - e^0(T)]\cdot K^2\cdot[\varepsilon - \eta - e^0(T)] + \tfrac{1}{2}\eta\cdot K^1\cdot\eta + cT(1 - \log T). \tag{16}$$

Example 2. Standard Elastoplasticity

The case of rheology is sufficiently similar: it suffices to replace K^1 by 0 and V by a rigid element with plastic deformation η, more traditionally denoted ε^P. One thus obtains

$$D = \sigma \cdot \dot{\varepsilon}^P$$

$$W = \frac{1}{2}[\varepsilon - \varepsilon^P - e^0(T)] \cdot K^2 \cdot [\varepsilon - \varepsilon^P - e^0(T)] + cT(1 - \log T).$$

We return, now, to eq (10); the reversible terms evaluate in this case as before to

$$-T(l \cdot \dot{\varepsilon} + m \cdot \dot{\eta}) = -T\frac{de^0}{dT} \cdot K^2 \cdot (\dot{\varepsilon} - \dot{\eta}) = -T\frac{de^0}{dT} \cdot (\sigma + K^2 \cdot \frac{de^0}{dT}\dot{T})$$

so that equation (10) is now written

$$c\frac{\partial T}{\partial t} - \text{div}(k \cdot \text{grad } T) = -T\frac{de^0}{dT} \cdot \dot{\sigma} + D + \phi \qquad (17)$$

where in the first term, c is the volumetric specific heat with zero stress.

This result is not limited to the preceding examples: it is easily shown that it extends to those solids for which the Helmholz Free Energy W is of the form

$$W(\varepsilon,\eta,T) = W_1(\varepsilon-\varepsilon^0,\eta) + f(T), \qquad (18)$$

that is, generally, to those which may be represented by a model of the preceding type with coefficients independent of temperature. One then has

$$c = c_{\varepsilon,\eta} + \frac{de^0}{dT} \cdot \frac{\partial^2 W_1}{\partial\varepsilon\partial\varepsilon} \cdot \frac{de^0}{dT}T.$$

2.2 Flat Plate Approximation

An IR camera cannot, of course, measure the interior temperature of an object, but only its surface temperature. Therefore, in general, the information of significance to mechanics does not appear except by inference which follows the solution of an inverse problem. Nevertheless, the temperature may often be considered practically uniform through the thickness of a flat plate; one may then treat the situation as a two-dimensional solid. and an IR camera provides access to the temperature field in the plan domain.

It is not our purpose here to discuss definitively the quality of the flat plate approximation in general, but simply to show that the equation for the thermal field in a homogeneous and isotropic flat plate subject to plane stess is of the form

$$\frac{\partial\theta}{\partial t} - d\left(\frac{\partial^2\theta}{\partial x^2} + \frac{\partial^2\theta}{\partial y^2}\right) + \frac{1}{\tau_{th}}\theta = -\alpha\,\text{tr}(\dot{\sigma}) + \frac{D}{c} \qquad (19)$$

and to evaluate the order of magnitude of the different terms.

We consider, in effect, such a plate (Fig. 3) of thickness e with its front face situated on the plane z=0; the tensor of conductivity and that of dilitation ($\partial e^0/\partial T$) are then scalars, and we can write

$$\alpha = \frac{T}{c}\frac{de^0}{dT}, \quad d = \frac{k}{c} \quad \text{(thermal diffusivity)}$$

We further consider our interest to be in small variations of temperature (a few degrees) around a reference temperature T_0 obtained, for example, when the plate is in thermomechanical equilibrium: stresses, strains and temperature are independent of time, and (17) is written as

$$-d\left(\frac{\partial^2\theta}{\partial x^2} + \frac{\partial^2\theta}{\partial y^2} + \frac{\partial^2\theta}{\partial z^2}\right) = \phi.$$

Since the coefficients α, c, and k vary little with temperature, and since the thickness is small, it is reasonable to assign to these coefficiernts, at the point (x,y,z), the values which they have at temperature

$T_0(x,y,0)$; thus, they become functions of x and y only.

The difference, $T' = T - T_0$ is the solution of

$$\frac{\partial T'}{\partial t} - d\left(\frac{\partial^2 T'}{\partial x^2} + \frac{\partial^2 T'}{\partial y^2} + \frac{\partial^2 T'}{\partial z^2}\right) = -\alpha\, tr(\dot{\sigma}) + \frac{D}{c} \qquad (20)$$

Now define

$$\theta = \frac{1}{e}\int_{-e}^{0} T'(x,y,z,t)\,dz$$

and take the mean value of both sides of (20)

The left-hand side produces the expression

$$\frac{\partial \theta}{\partial t} - d\left(\frac{\partial^2 \theta}{\partial x^2} + \frac{\partial^2 \theta}{\partial y^2}\right) + \frac{1}{ec}\left[k\frac{\partial T'}{\partial z}(x,y,-e) - k\frac{\partial T'}{\partial z}(x,y,0)\right]$$

where the term within the square brackets is the flux of heat lost by the plate through the front and back faces. If T' is small, the square brackets are, in general, equal to a linear function of $T'(x,y,-e)$ and $T'(x,y,0)$ through linearization about T_0 of the laws of conduction, convection and radiation. Moreover, $T'(x,y,-e)$ and $T'(x,y,0)$ may be approximated by θ such that the preceding expression is identical to the left-hand side of (19). The constant τ_{th} has the dimension of time; in the case where the effects of convection and conduction may be neglected, this constant is given by the Stefan-Boltzmann law

$$q = \text{emiss} \times \sigma_E T^4$$

where q designates the radient flux, emiss the emissivity (equal to 1 for a black body), and σ_E is the constant

$$\sigma_E = 5.67 \times 10^{-8}\ W/m^2/°K^4.$$

On linearizing about T_0, one obtains

$$\frac{1}{\tau_{th}} = \frac{\text{emiss}}{ec} 8\, \sigma_E T^3 \qquad (21)$$

which is, for a black body at 300K

$$\tau_{th} = ec \times 12.25 \text{ sec.} \qquad (22)$$

For common materials, τ_{th} = is on the order of hundreds of seconds per millimetre of thickness. When the plate is in contact with air, convection can reduce τ_{th} to around ec/10 or even to ec/50. Therefore, one may wish to perform experiments in a partial vacuum to eliminate convection.

Under the plane stress hypothesis, the stress tensor σ and that of strain ε are independent of z, while the components σ_{13}, σ_{23} and σ_{33} are zero. The dissipation D is thus also independent of z, and finally, one obtains equation (19).

2.3 Some orders of magnitude.

To fix these concepts, we assign numerical values to the various constants which appear in (19), for a black plate 1 mm in thickness and constituted of one or the other of the two quite different materials, titanium or plexiglas. The temperature T_0 is room temperature: 300K. To estimate the terms a tr (s) and D which occur in (19), one considers the two materials to be pulled within their linear domains, with the variations of stress σ, to be simple tension or compression σ_m and $-\sigma_m$, σ_m designating the elastic limit in tension. This permits the comparison of the two selected materials despite their great dissimilarity. We introduce tan ϕ, ϕ designating the conventional loss angle, that is the phase between strain and stress under harmonic motion

of frequency f_t. D is calculated under the hypothesis of such a motion at a single frequency f_t remote from a "peak of internal friction." One has

$$D(t) = E^{-1}\sigma_m^2 2\pi f_t \tan\phi \sin^2(2\pi f_1 t) \tag{23}$$

and it is in fact the quantity

$$\bar{\delta\theta} = \frac{E^{-1}\sigma_m^2}{c}\pi \tan\phi \quad (E: \text{Young's Modulus}) \tag{24}$$

which is observed: this is the elevation in temperature caused by dissipation during one period in a volume element having zero heat loss. Likewise, the quantity

$$\hat{\delta\theta} = 2\alpha\sigma_m \tag{25}$$

represents the total temperature variation produced during one cycle by the "isentropic" term $\alpha\, tr(\dot{\sigma})$.

One notes that the "isentropic" variations of temperature, that is $d\hat{\theta}$ are, during the course of a single cycle of magnitude 1000 times (titanium) or 20 times (plexiglas) greater than the elevation of temperature $\delta\theta$ due to dissipation when the maximum stress is the elastic limit.

Quantity	Units	Titanium	Plexiglas
c	$(j/m^3)/^oK$	2.35×10^6	1.76×10^6
k	$(W/m)/^oK$	21.75	0.188
d	m^2/s	9.26×10^{-6}	0.107×10^{-6}
$\partial e^0/\partial T$	$^oK^{-1}$	8.9×10^{-6}	80×10^{-6}
α	^oK/pascal	1.14×10^{-9}	13.6×10^{-9}
σ_m	hectobars	35	5
E	hectobars	10550	300
$\tan\phi$	1	0.5×10^{-3}	40×10^{-3}
$\delta\theta$	^oK	0.78×10^{-3}	60×10^{-3}
$\delta\theta$	^oK	0.80	1.35
τ_{th}/e	sec/mm	192	144

These values apply at maximum stress; for smaller values, $\delta\theta$ varies with the maximuim stress and $\delta\theta$ with its square.

3. OBSERVATIONS OF OSCILLATIONS OF A PLATE

The preceding numerical values indicate sufficiently clear discrimination between the isentropic variations of temperature, which are observed on a time scale short with respect to $1/f_t$ and the average heating, which is observed on a time scale long with respect to τ_{th}, to the extent that a stationary regime is obtained for which the heat loss associated with temperature increase removes the heat generated by dissipation.

We thus consider a flat plate subject to oscillating forces in its plane of frequency f_t. If this is clearly lower than the frequency of the gravest plate mode, the mechanical force regime is attained in a few periods; if we assume further that the small temperature increase does not change the conditions for dissipation, by causing, for example, the onset of plastic deformation, one may further consider the right-hand side of (19), which we

shall call q, to be a periodic function with period f_t^{-1}. It is conventional to decompose this function as

$$q = \bar{q} + \hat{q}, \quad \bar{q} = f_t \int_0^{f_t^{-1}} q(t)\,dt \tag{26}$$

One further finds

$$\hat{q} = -\alpha\, tr(\dot{\sigma}) + \frac{\hat{D}}{c}. \tag{27}$$

Although the temperature θ is not *a priori* a periodic function of time, one may still put

$$\theta = \bar{\theta} + \hat{\theta}, \quad \bar{\theta}(t) = f_t \int_t^{t+f_t^{-1}} \theta(\xi)\,d\xi \tag{28}$$

which separates the "slow" part $\bar{\theta}$ from the "fast" part $\hat{\theta}$.
One can show that (19) separates into two equations as follows

$$\frac{\partial \bar{\theta}}{\partial t} - d\nabla_H^2 \bar{\theta} + \frac{\bar{\theta}}{\tau_{th}} = \frac{\bar{D}}{c} \tag{29}$$

$$\frac{\partial \hat{\theta}}{\partial t} - d\nabla_H^2 \hat{\theta} + \frac{\hat{\theta}}{\tau_{th}} = -\alpha\, tr(\dot{\sigma}) + \frac{\hat{D}}{c}. \tag{30}$$

where ∇_H^2 denotes the bidimensional Laplacian

$$\nabla_H^2 \equiv \frac{\partial^2}{\partial x^2} + \frac{\partial^2}{\partial y^2}$$

This separation is valid under the conditions of linearity which we have assumed.

Evolution of the mean temperature $\bar{\theta}$

This is governed by equation (29). If one assumes that τ_{th} is non-zero, then (29) certainly has one solution of constant θ_∞. We note that if τ_{th} is zero, this existance may still be assured by virtue of the limits allowed on removal of heat supplied by $\bar{D}$. Conventional inequality analysis then allows us to write

$$\| \bar{\theta}_\infty - \bar{\theta}(t) \| \leq \exp\left(-\frac{t}{\tau_{th}}\right) \| \bar{\theta}_\infty - \bar{\theta}(0) \| \tag{31}$$

and an inequality of the same type (obtained using Gronwall's lemma) in the case where τ_{th} is zero and the temperature is fixed on the boundaries.

Applying a spatial Fourier† Transform $\mathcal{F}_{x,y}$ one can write equation (29) in the form,

$$\frac{\partial \bar{\Theta}_{x,y}}{\partial t} + \left[d(f_x^2 + f_y^2) + \frac{1}{\tau_{th}}\right]\bar{\Theta}_{x,y} = \frac{1}{c}\mathcal{F}_{x,y}(\bar{D})$$

and the same technique of inequality analysis produces, under this

† In the case of a finite plate, one should, in all rigor, use a finite Fourier transform, that is, the Fourier transform of the product of θ and a "bounding window" whose opening is occupied by the plate. One reaches the same conslusions.

transformation

$$\| \bar{\Theta}_{\infty,x,y} - \bar{\Theta}_{x,y}(t) \| \leq \exp\left(- t \left[d(f_x^2 + f_y^2) + \frac{t}{\tau_{th}} \right] \right) \| \bar{\Theta}_{\infty,x,y} - \bar{\Theta}_{x,y}(0) \| \quad (32)$$

generalizing (31) and showing that the limiting regime is attained very rapidly for the high spatial frequencies f_x and f_y.

Evolution of the term with zero mean value $\hat{\theta}$

It is interesting to compare the orders of magnitude of the terms directly. A spatial and temporal Fourier transform $F_{x,y,t}$ of (30) thus produces

$$\left[j2\pi f_t + 4\pi d (f_x^2 + f_y^2) + \frac{1}{\tau_{th}} \right] \hat{\Theta}_{x,y,t} = - j2\pi f_t \alpha \, tr(F_{x,y,t}(\sigma)) + \frac{1}{c} F_{x,y,t}(\hat{D}). \quad (33)$$

In the absence of diffusion, loss through the faces and dissipation, only the first term remains on each side of the equation, and the temporal variation of temperature proportional to that of stress is written as

$$\hat{\Theta}_{x,y,t} = - \alpha f_t tr(F_{x,y,t}(\sigma)).$$

We evaluate the order of magnitude of the other terms as perturbations to these phenomena. It was previously shown that on the right-hand side, $\hat{D}$ was of the order of D since the temperature variations during a cycle are much smaller than the variations of the type $\delta\hat{\theta}$. On the left-hand side, $1/\tau_{th}$ is on the order of 10^{-2}, practically negligible in comparison with $2\pi f_t$. It is more interesting to calculate the temporal frequency f_t, at which one can justify neglecting diffusion.

Suppose that we observe an image of diameter 50 mm and that we want to distinguish details on the order of a half millimetre, that is, a very precise image. Thus

$$\sqrt{f_x^2 + f_y^2} = 2 \times 10^3 m^{-1}.$$

This accomplished, if one wishes that the diffusion terms be about one percent of the leading terms, then

$$f_t \geq 8\pi d 10^6 = \begin{cases} 23200 \text{ Hz for titanium} \\ 270 \text{ Hz for plexiglas} \end{cases}$$

which are frequencies easily obtainable in the laboratory, and substantially below the lowest resonant frequencies, which are on the order of 100 KHz for a plate of titanium and ablut 31 KHz for one of plexiglas. This indicates the possibility of using the isentropic effect as a basis for a new technique of extensometry on thin objects which are subject to quasi-steady oscillations.

Although the preceding estimates seem reassuring concerning the orders of magnitude of the various terms, a point yet remains to be settled: May one hope to obtain sufficient precision such that the theoretical possibilities which one glimpses correspond to potentially accessible techniques? It is this which we proceed to examine in the following paragraphs.

4. VARIOUS EXAMPLES OF APPLICATION OF THERMOGRAPHY TO MECHANICS

We wish first to describe an application for which thermomechanical coupling is not a cause: thermograms sometimes permit detection of certain anomalies in the thermal field for which the cause is geometrico-mechanical, as, for example, the presence of a crack. If this is open, thus essentially

non-conducting to heat, the propagation of heat will conform to the shape of the obstacle, and so strongly perturb the temperature field. It is this which one observes in the thermogram of figure 4, which represents a thin plate: a crack has been artificially introduced, and one clearly sees its effect on the thermal field since the temperature indicates a discontinuity. Applications of this type are already in the process of industrial development, and techniques of signal analysis and pattern recognition are expected to prove fruitful.

The study of isentropic temperature variations has been pursued from the point of view of stroboscopy by Blanc and Giacometti [8]; the problem of precision undoubtedly requires a stroboscope at two points over one period in a fashion to eliminate the derivative of θ. In effect, if one considers that the signal which gives θ is swamped by noise of zero mean and standard deviation of about 0.1°C. one realizes that it requires about 100 measurements to bring the error to the vicinity of 1/100 °C. The derivative of $\bar{\theta}$ is not more negligible, as that is the desired order of precision, even for a material with small dissipation. One sees that a device for rapid digitization of the signal is necessary.

We expand further the applications to those which particularly involve the effects of dissipation. Various thermograms have already been published by [6], who show plan view modes of vibration of diverse objects which are excited by ultrasonic transducers, loudspeakers, plates in flexural vibration, etc. But the quantitative information supplied in these first published examples has remained very meager, no rapid digitization apparently having been employed. In contrast, we give in the following paragraph an example where, thanks to a relatively primitive digitizer, one may identify the sources of heat corresponding to plastic deformation in the vicinity of a crack tip.

5. LOCATION OF THE PLASTIC DISSIPATION IN THE VICINITY OF THE TIP OF A FATIGUE CRACK

We mounted a sample of titanium 60 mm wide and 0.5 mm thick on a tensile fatigue machine, and subjected it to cyclic oscillations at a frequency of 10 Hz. A saw cut initiated a crack, the progression of which we followed with the aid of an AGA680 camera to obtain the photographs in Fig. 5 and 6, which show the field for the entire width. One distinguishes very quickly the heating $\bar{\theta}$ at the head of the crack, and the same photographs, which correspond respectively to the instants of minimum and maximum tension, also show the variation of $\hat{\theta}$ over the course of a cycle. The progression of the crack is very slow, on the order of 1 mm per 1000 cycles; on the other hand, the spatial resolution (98 points per line, 70 lines per image) is relatively small. In sum, one may consider the observed regime to be stationary and assume that $\bar{\theta}$ satisfies

$$-d\nabla_H^2\bar{\theta} + \frac{\bar{\theta}}{\tau_{th}} = \frac{\bar{D}}{c} . \tag{34}$$

One can thus evaluate the temperature $\bar{\theta}$ and eliminate $\hat{\theta}$ by an appropriate choice of sampling frequency, and the correct value for $\theta(x_i,y_j)$ is, in fact, the arithmatic mean of N measurements of $\theta(x_i,y_j,t)$ obtained at the point (x_i,y_j) for which the phase values are uniformly distributed between 0 and 2π. Here, N equals 100. The field of temperature θ thus obtained is shown in figures 7 and 8.

$$\nabla_H^2\theta_{est}(x,y) = \iint \phi(x',y')\,\nabla_H^2\bar{\theta}_{obs}(x-x',y-y')\,dx'dy' \tag{35}$$

(see [11] for details.)

The size of the significant extent of ϕ provides the order of magnitude of the spatial resolution obtainable by this estimate. More precisely, these result from a low-pass filter of $\nabla_H^2 \bar{\theta}_{obs}$, as we see a little further on.

By a classical property of convolutions, one has in consequence

$$\nabla_H^2 \bar{\theta}_{est}(x,y) = \iint \nabla_H^2 \phi\ (x',y') \times \bar{\theta}_{obs}(x-x',y-y')\,dx'dy' \tag{36}$$

which is descretized to the form

$$\nabla_H^2 \bar{\theta}_{est}(x,y) = \sum_{\substack{-I \le i' \le I \\ -J \le j' \le J}} \nabla_H^2 \phi(i'\Delta x, j'\Delta y) \times \bar{\theta}_{obs}((i-i')\Delta x, (j-j')\Delta y), \tag{37}$$

the formulation leading to the results seen in Figure 9.

The estimate of (37) differs from the actual $\nabla_H^2 \bar{\theta}$ by an error which arises from three sources.

(a) Error from folding the spectrum (in English, aliasing). It is well-known that sampling an actual signal leads to a systematic error if the sampling frequency is not at least two times greater than the highest frequency contained in the signal. This type of error is much reduced here, for the field of temperature θ has previously been concentrated in the lower spatial frequencies. Furthermore, the signal has been filtered by the digitizer.

(b) Errors in filtering. The Fourier transform of (35) gives

$$\mathcal{F}\{\nabla_H^2 \bar{\theta}_{est}\}(f_x,f_y) = \mathcal{F}\{\phi\}(f_x,f_y)\,\mathcal{F}\{\nabla_H^2 \bar{\theta}_{obs}\}(f_x,f_y) \tag{38}$$

As a simple example†, suppose that we have selected $\Phi = \mathcal{F}(\phi)$ as the product of Hamming windows in f_x and f_y. Let Φ_H be the one-dimensional window

$$\Phi_H(\rho) = \begin{cases} 0.56 + 0.44 \cos 2\pi\rho & \text{for } -\frac{1}{2} \le \rho \le \frac{1}{2} \\ 0 & \text{for } |\rho| > \frac{1}{2} \end{cases} \tag{39}$$

Accordingly, one takes $f_{x,e}$ and $f_{y,e}$ to be the spatial sampling frequencies along x and y.

$$\Phi(f_x,f_y) = \Phi_H(f_x/f_{x,e})\,\Phi_H(f_y/f_{y,e})$$

The inverse transform to Φ is easily calculated, along with its Laplacian. One establishes that it is sufficient to limit, in (39), I=J=6, which defines the effective volume of calculation for the convolution. Elsewhere, one sees that (38) and (39) show the filtering error. If, for example, one accepts no more than 10% error of this type, one should be interested in only those spatial frequencies f_x and f_y such that

$$(0.56 + 0.44 \cos 2\pi \frac{f_x}{f_{x,t}})(0.56 + 0.44 \cos 2\pi \frac{f_y}{f_{y,t}}) \ge 0.9$$

which gives, if one chooses the same limit of ρ_{max} for the two axes $f_x/f_{x,e}$ and $f_y/f_{y,e}$: $\rho_{max} \approx 0.08$.

In past tests, the spatial frequency in x and in y has been on the order of 1.6 mm^{-1}, such that only details of diameter on the order of $(1/2)(0.08 \times 16)^{-1} \approx 4$ mm can be observed with a filtering error less than 10%. In optical terms, the resolution, for an error of 10%, is approximately a pair of lines every eight millimetres, which is weak.

†In reality, one uses a window of revolution where the "meridian" is a Hamming window

(c) Errors from noise. Consider each temperature measurement to be associated with a random error with zero mean value and a standard deviation $\delta\theta$ which applies to every measured point. Consider further that the errors between two different measured points are independent random variables.

Then the estimate $\nabla_H^2 \bar{\theta}_{est}$ obtained with formula (37) is associated with a random error of zero mean and standard deviation

$$\delta(\nabla_H^2 \bar{\theta}) = \frac{\delta\theta}{\sqrt{N}} \left\{ \sum_{i'j'} [\nabla_H^2 \phi(i'\Delta x, j'\Delta y)]^2 \right\}^{1/2} \tag{40}$$

In our previous experience, as has been noted above, N=100 while $\delta\theta$ is the raw resolution in temperature which, as was noted at the beginning of the study, is about 0.2 C. This gives for $\bar{\theta}$ a standard error of 0.02 C and, after application of (40), a standard error for $\nabla_H^2 \bar{\theta}$ of

$$\delta(\nabla_H^2 \bar{\theta}) = 0.038\,°C/mm^2 \tag{41}$$

One may then write (34) below as

$$-\nabla_H^2 \bar{\theta} + \frac{\bar{\theta}}{d\tau_{th}} = \frac{D}{k} \tag{42}$$

Even if natural convection considerably lowers τ_{th} with respect to values calculated for radiation from the faces, τ_{th} remains greater than 0.2 sec for the cases studied. This limits the standard error $\delta(\bar{\theta}/d\tau_{th})$ to $0.01°C/mm^2$. In all, the standard error for the left-hand side of (42) is less than $0.05\,°C/mm^2$.

To estimate the quality of this approximation, suppose that, in the region under consideration of about 4 mm in diameter, the plastic deformation

$$\int_t^{t+T} |\dot{\varepsilon}_p| \, dt$$

is, on the average, 10^{-3} per period. For one case studied at 10 Hz, that gives, for mean dissipated power

$$\bar{D} = 10 \times 35 \times 10^7 \times 10^{-3}\ W/m^3$$

and the right-hand side of (42) equals

$$\frac{\bar{D}}{k} = 0.161\ °C/mm^2$$

so that the standard error for the measurement of the right-hand side is on the order of 30%.

Such a result is still very interesting in comparison with the possibilities of traditional techniques, as, for example, the diffraction χ. But it needs to be considerably improved.

1. By an optimal choice of optics, permitting the observer to concentrate on the zone of interest, thereby considerably reducing the filtering errors.

2. With a rapid digitizer, to augment simultaneously the sampling frequency and the number N of obtainable measurements.

3. To perform experiments under partial vacuum in order to eliminate convection losses and concomitantly the uncertainty in the term $(\bar{\theta}/d\tau_{th})$, very difficult to control.

One hopes, thus, instead of an analog experiment described here, to bring the standard error to a few percent for a spatial resolution on the order of a millimetre.

Figure Captions

Fig 1. Linear viscoelastic solid with dilitation.

Fig 2. Ideal elasto-plastic solid with thermal dilitation e_0.

Fig 3. Thin plate "observed" on face B.

Fig 4. Thermogram of a cracked plate

Fig 5. Thermogram of the progression of a fatigue crack. IR stroboscopy at minimum stress.

Fig 6. Thermogram of the progression of a fatigue crack. IR stroboscopy at maximum stress.

Fig 7. Progression of a fatigue crack. Image is digitized and reassembled following noise removal.

Fig 8. (a) Thermal profile (noisy) along the crack axis. (b) The same profile averaged over ten frames. (c) The same profile averaged over 50 frames. (d) The same profile averaged over 100 frames.

Fig 9. Source of heat at the tip of a fatigue crack obtained by numerical filtering of the temperature data in Fig 7.

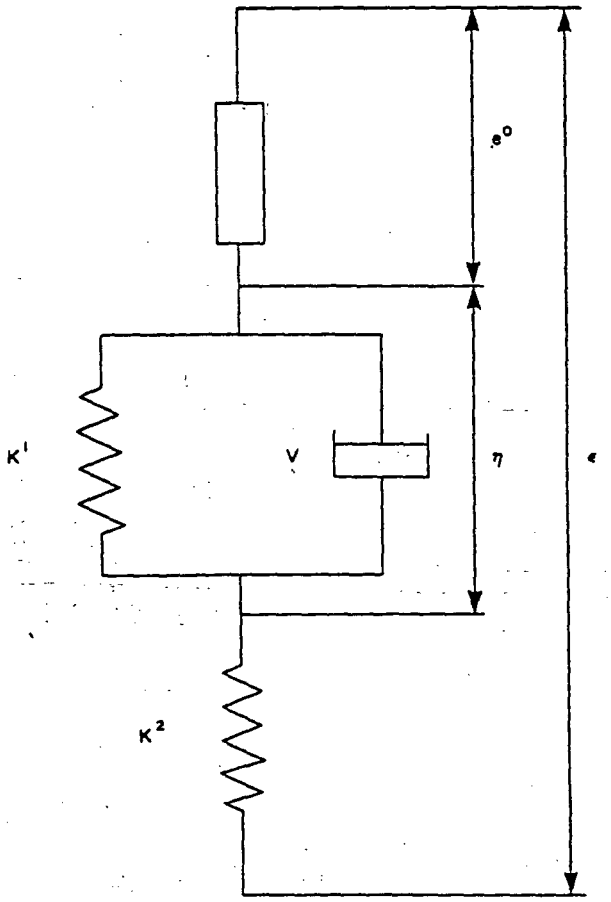

Fig. 1. Solide viscoélastique linéaire avec dilatation thermique e_0.

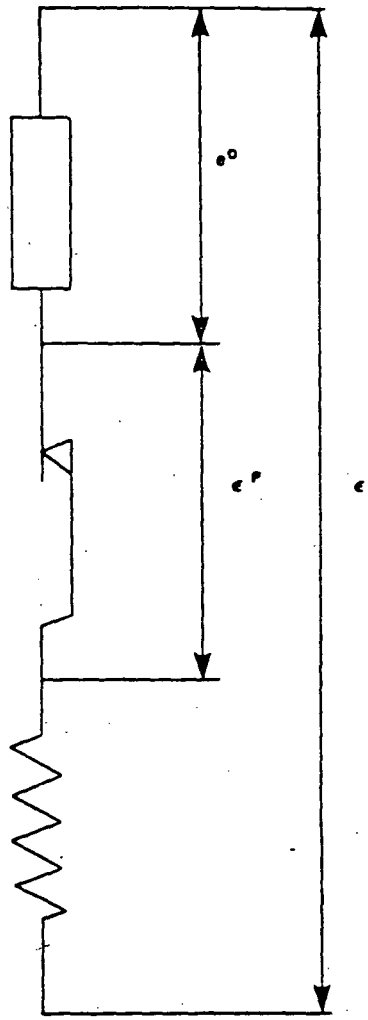

Fig. 2. Solide élasto-plastique parfait avec dilatation thermique e_0.

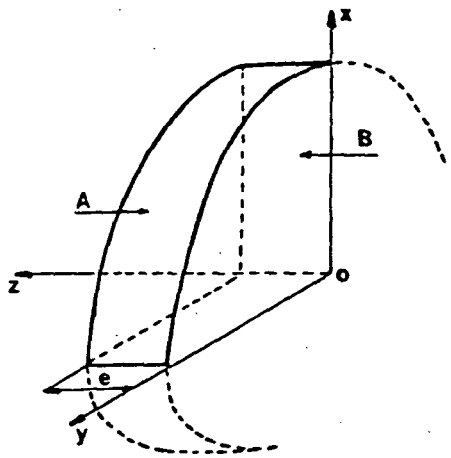

Fig. 3. Plaque mince "observée" sur la face *B*.

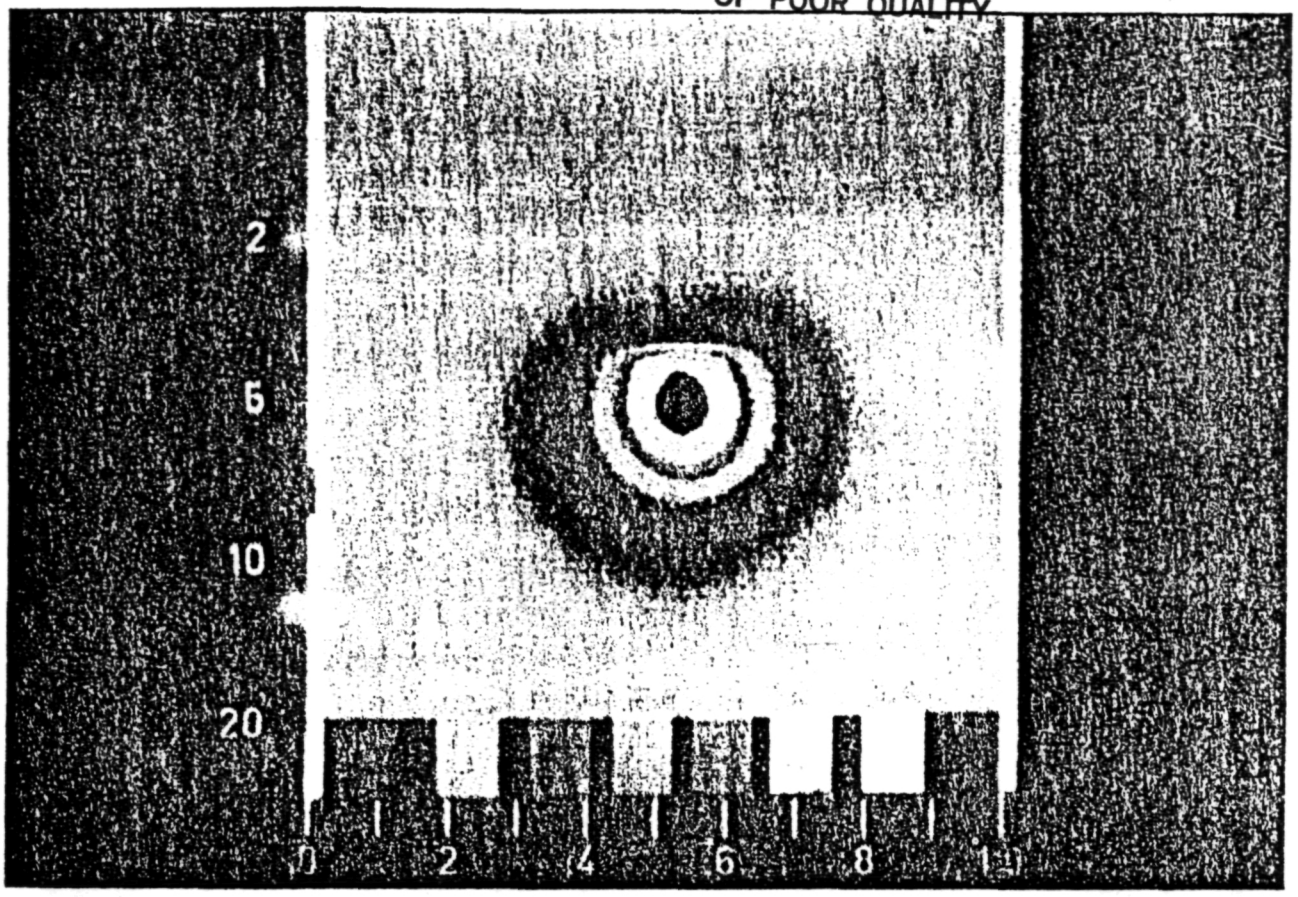

Fig. 4. Thermogramme de plaque fissurée.

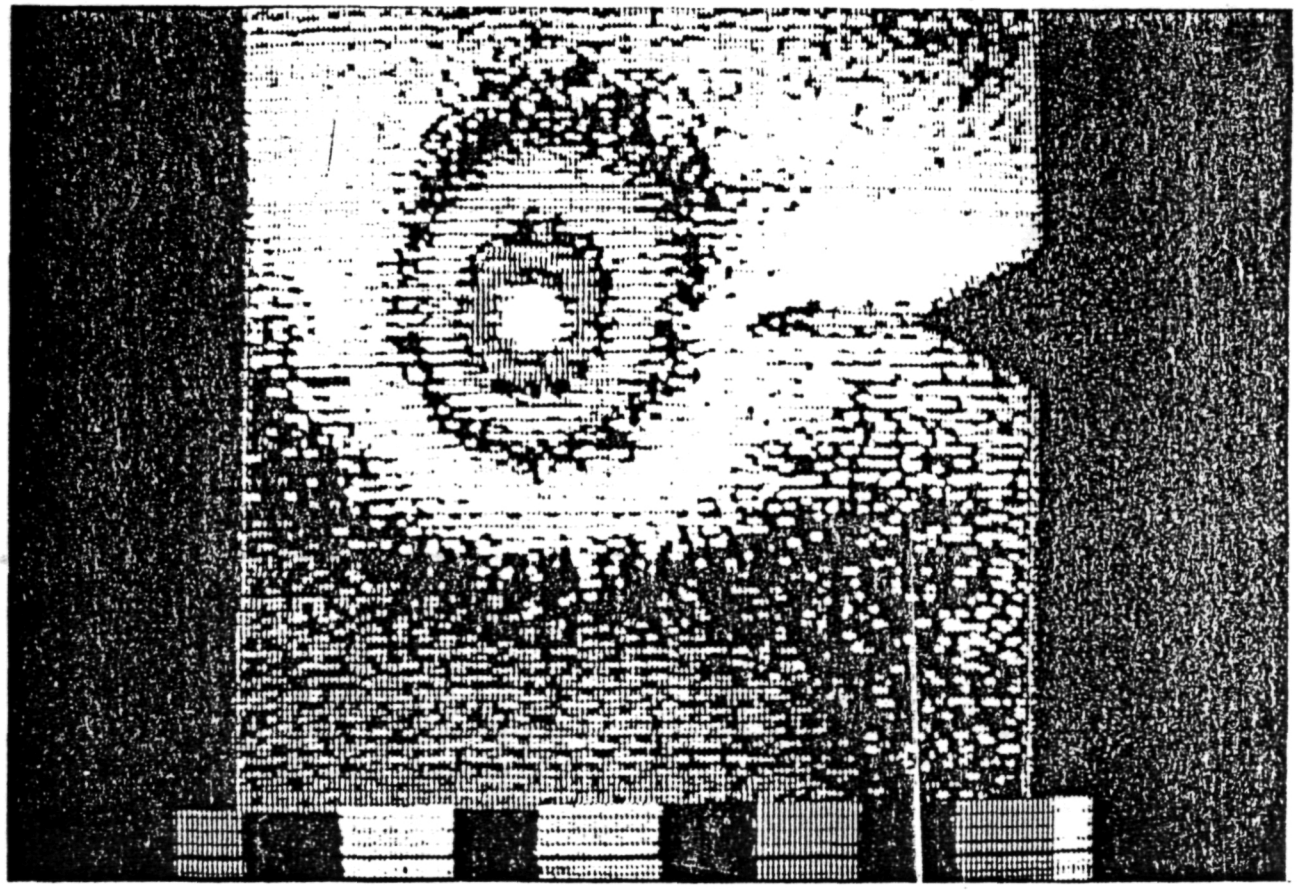

Fig. 5. Thermogramme de progression d'une fissure de fatigue. Stroboscopie IR sur l'effort minimal.

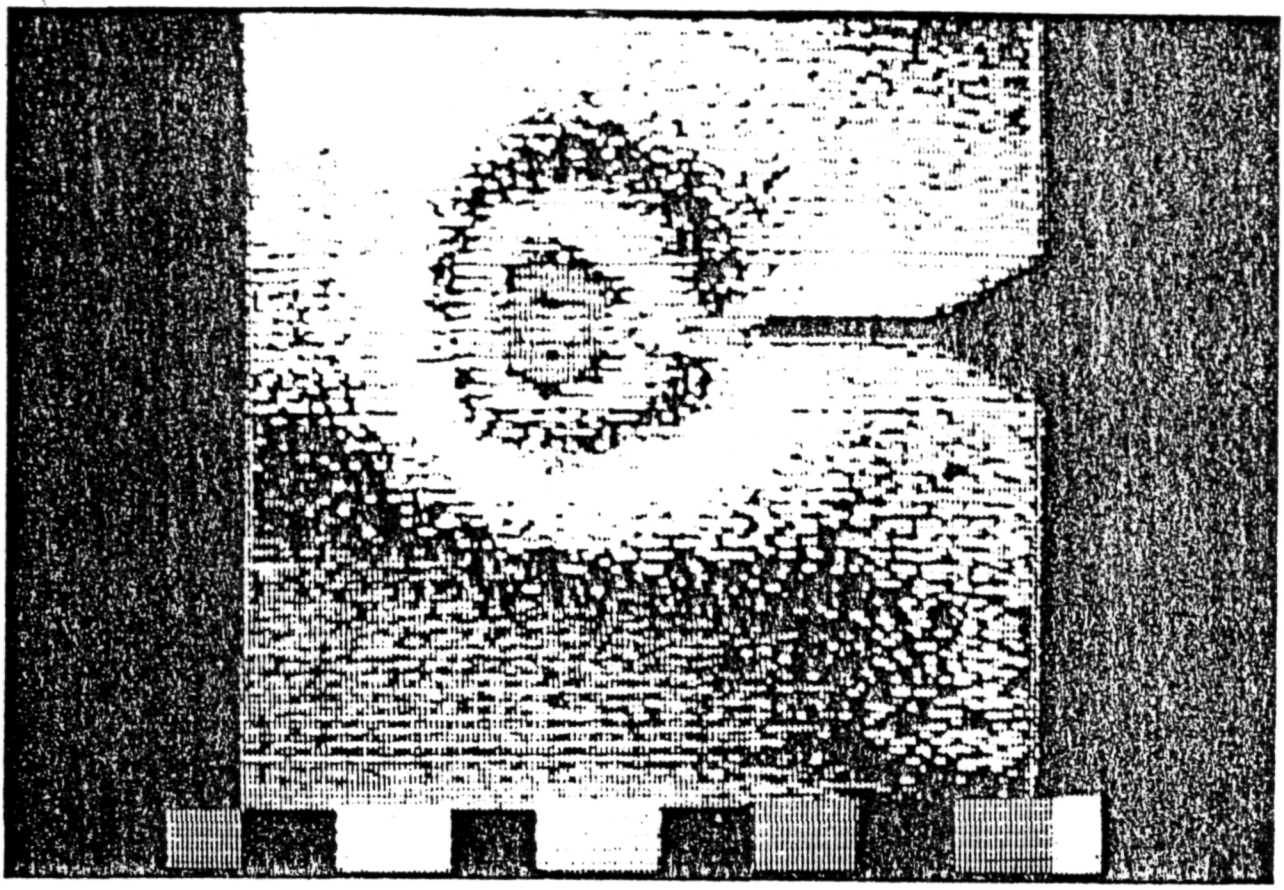

Fig. 6. Thermogramme de progression d'une fissure de fatigue. Stroboscopie IR sur l'effort maximal.

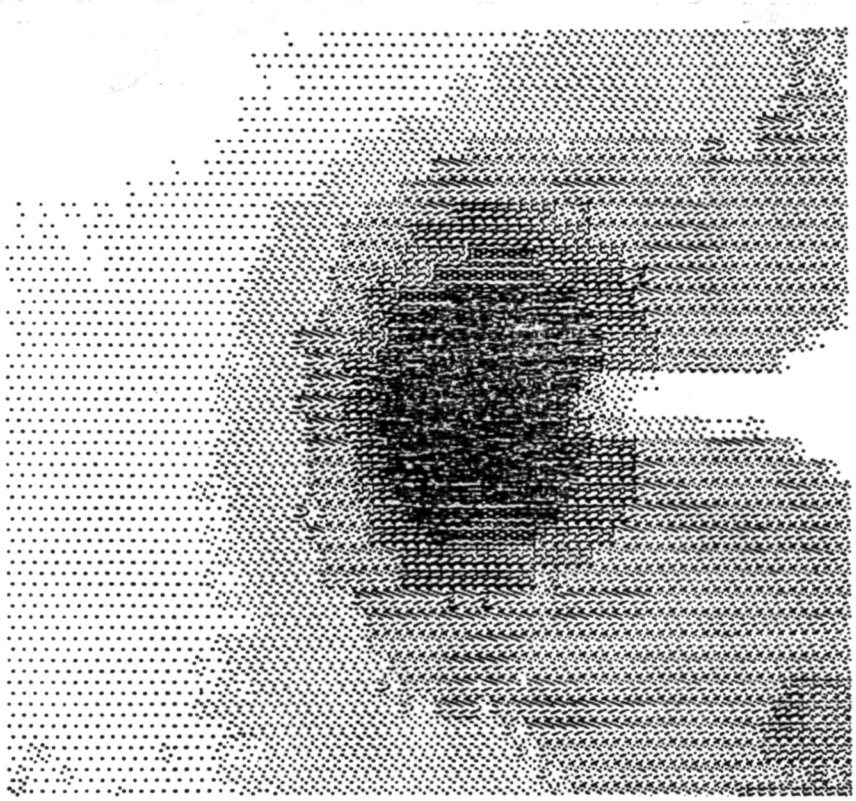

Fig. 7. Progression d'une fissure de fatigue. Image numérisée et reconstituée après débruitage.

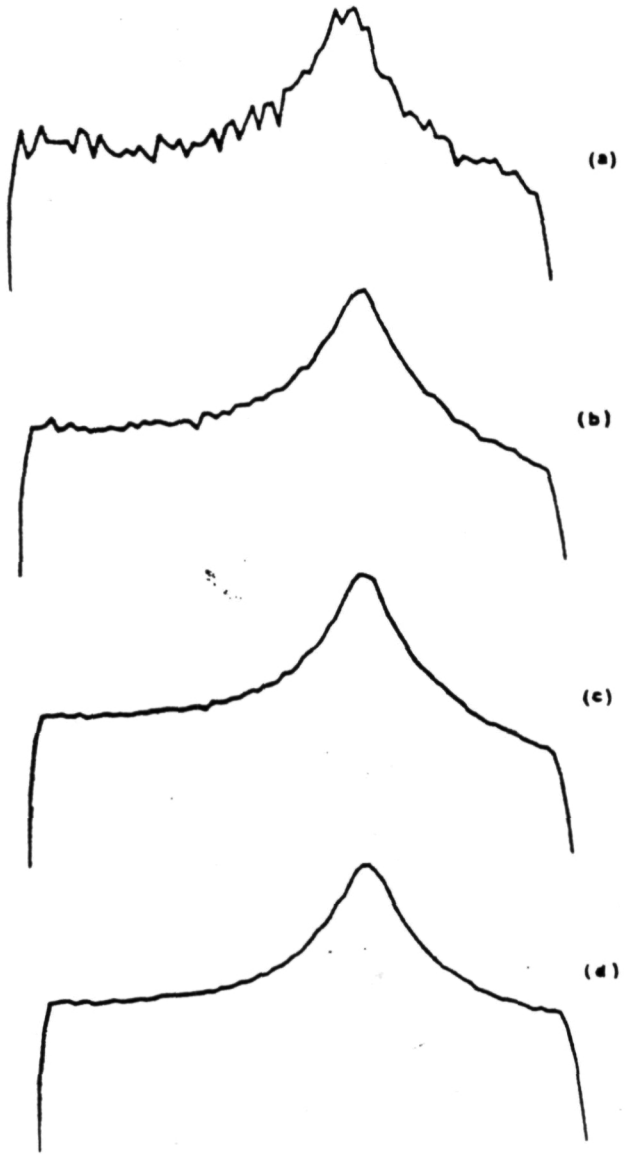

Fig. 8. (a) Profil thermique (bruité) dans l'axe de la fissure. (b) Même profil après moyenne sur 10 trames, (c) Même profil après moyenne sur 50 trames, (d) Même profil après moyenne sur 100 trames.

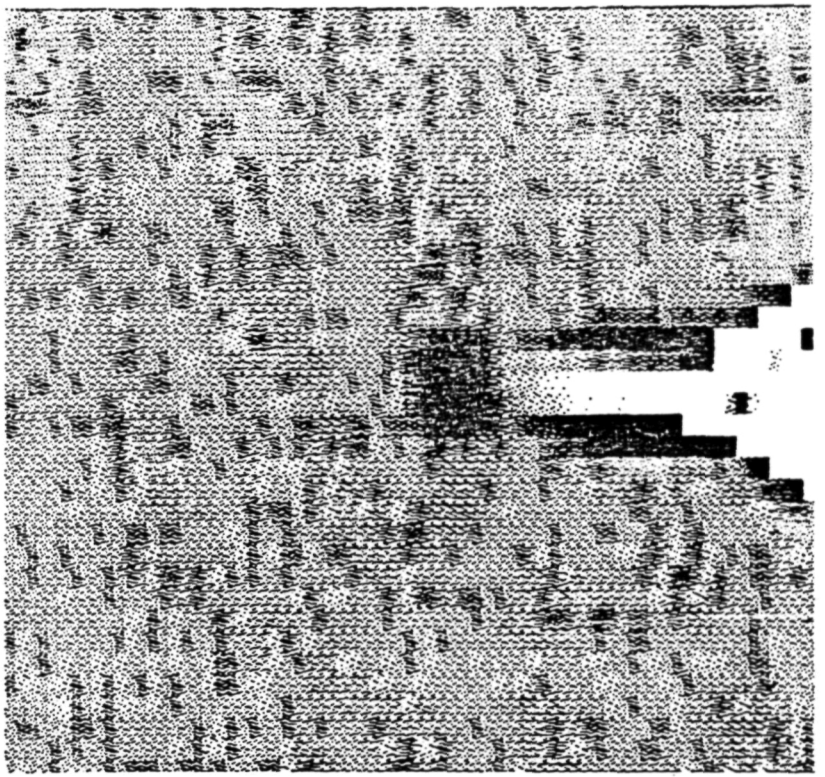

Fig. 9. Source de chaleur en tête d'une fissure de fatigue obtenue par filtrage numérique des données température de la Fig. 7.